1 **Pressure, temperature and timing of mineralization of the**

2 **sedimentary rock-hosted orogenic gold deposit at Klipwal,**

3 **southeastern Kaapvaal Craton, South Africa**

4

5 **Sakthi Saravanan Chinnasamy[1*$], Ron Uken[1#] Jürgen Reinhardt[1], David Selby [2],**

6 **Spencer Johnson[3]**

7

8 [1]School of Agricultural, Earth and Environmental Sciences, Discipline of Geological

9 Sciences, University of KwaZulu-Natal, Westville Campus, Durban 4000, South

10 Africa

11 [2]Department of Earth Sciences, University of Durham, Durham DH1 3LE, UK

12 [3]No 326, Canterbury Ct., Alamo, CA, 94507, USA

13 *Corresponding author e-mail:geosaks@gmail.com

14 [$]Present address:
15 Department of Earth Sciences, CEMPEG, Uppsala University, Villavagen 16, SE-

16 75236 Uppsala, Sweden

17 [#] Present address:

18 17 N. Grosvenor Ave, Burnaby, V5B1J1, BC, Canada
19

20 **Abstract**

21

22   Gold mineralization in the Klipwal Shear Zone (KSZ) at the Klipwal Gold

23 Mine is confined to laminated quartz-carbonate lodes, stringers and associated

24 alteration in sandstone and siltstone of the Delfkom Formation in the upper Mozaan

25 Group of the Mesoarchaean Pongola Supergroup. The moderately dipping brittle-

26 ductile KSZ strikes N-S with an oblique-reverse, sinistral sense of shear. The

27 deformational events that are recognized include an early compressional phase that

28 produced anastomosing shears defined by shear fabrics with numerous shear-parallel

29 laminated quartz-carbonate fault-fill veins and, in places, extensional quartz vein

30 stockworks, and a late brittle reactivation phase that produced fault breccias,

31 displacing earlier extensional veins. Three closely spaced economic reefs (lodes) are

32 developed: the main R-reef constitutes the KSZ, while the J- and H- reefs represent

33 footwall splays. Alteration comprises chlorite, muscovite, epidote, feldspar and

34 carbonates along with pyrite, arsenopyrite and chalcopyrite $\pm$ pyrrhotite. An inner

alteration zone is dominated by laminated quartz-carbonate veins with alternating quartz-carbonate-rich and muscovite-chlorite-rich laminae whereas the proximal zone is characterized by alteration halos of K-feldspar, albite, epidote, chlorite and muscovite along with carbonates and associated quartz veins. Chlorite thermometry from the inner and proximal zone yielded temperatures of 267 to 312 °C. Arsenopyrite compositions provide temperatures in the same range, 255 to 318 °C. Fluid inclusion microthermometry and Raman spectrometry of quartz veins in the mineralized reefs reveal the presence of metamorphogenic aqueous-gaseous fluid with an average salinity of 6.5 wt. % NaCl equiv. Fluid compositions and estimated P–T range (1.1 to 2.5 kbar at 255 to 318 °C) are typical of orogenic gold deposits. Devolatilization during the regional facies metamorphism of the Pongola Supergroup is considered the likely fluid forming event with fluid flow focused into a 'compressional-jog' of the KSZ. Shear-induced pressure fluctuations generated phase separation of the initial aqueous gaseous fluid producing a gaseous and low saline aqueous fluid. This, together with fluid–rock interaction, and a decrease in fO_2 lead to sulphide and gold precipitation at Klipwal. Re-Os data from six sulfide samples constrain the age of sulfide precipitation and, by inference, gold mineralization, to 2563 ± 84 Ma, with an initial $^{187}Os/^{188}Os = 0.29 \pm 0.08$ (MSWD = 0.38). This age is distinctly younger than the post-Pongola granites (2863–2721 Ma) ruling out the association of granite emplacement with mineralization. This would suggest that mineralization is linked to the regional D_3 folding event which reactivated the KSZ after emplacement of the post-Pongola granites and that final brittle, post-mineralization reactivation is related to Karoo-age faulting. Low initial Os values suggest that ore fluid interacted with mafic rocks, leaching non-radiogenic Os, the likely source being the deeper-seated Nsuze Group volcanics and/or the greenstone belts that underlie the Pongola Supergroup.

Keywords: Orogenic gold deposits, Fluid inclusions, Klipwal, Kaapvaal craton, South Africa

Introduction

Orogenic gold mineralization constitutes an important class of deposits, collectively representing a significant world gold resource (about 25000 t gold; Goldfarb et al.

2005). Although these ores are associated with deformed metamorphic terrains of almost all ages (Kerrich and Cassidy 1994) they mostly occur in the Archaean greenstone belts of Australia, Canada, Africa, India and Brazil, the Proterozoic belts of West Africa, and to a lesser extent, in Mesozoic and Cenozoic provinces (Kerrich and Cassidy 1994; Goldfarb et al. 2001; Groves et al 2003; Hagemann and Brown 2000). They are characterized by a strong structural control, distinct alteration assemblages, ore mineralogy, ore fluid composition, and occur in a range of host lithologies (Groves et al. 1998; McCuaig and Kerrich 1998; Goldfarb et al. 2001; Groves et al. 2003). These include greenstones (metamorphosed from low greenschist facies to granulite facies), banded iron-formations, ultramafic rocks, sedimentary rocks and granitoids (McCuaig and Kerrich 1998, and references therein). Among all these, sedimentary rock-hosted orogenic lode gold deposits form an important and distinctive class (Bierlein and Crowe 2000).

Although the sedimentary rock-hosted deposits are well known from the Phanerozoic there are only a handful from the Archaean, which in many ways are similar in mineralization and structural style, alteration and ore mineralogy to the Phanerozoic counterparts. These deposits, also called slate belt-hosted gold deposits, are developed in mineralized shear zones in thick marine sedimentary sequences commonly underlain by bimodal volcanics generated during spreading, arc formation, plate collision and subduction (Goldfarb et al. 1998). They are associated with major translithospheric structures or compressional to transpressional-transtensional shear zones, similar to the Archaean orogenic gold deposits (Bierlein and Crowe 2000; Lawley et al. 2013).

Sedimentary rock-hosted orogenic gold deposits are reported from a number of Phanerozoic accretionary terrains, notably the Pacific rim: the North American Cordillera, far east Russia, northeastern China, eastern Australia and New Zealand (Fig. 1 in Goldfarb et al. 1998; Bierlein and Crowe 2000). Some of the major gold-bearing districts in the eastern and western part of the Pacific rim include the Hodgkinson gold field in the Hodgkinson–Broken River Fold Belt and Ballarat in the Lachlan Fold Belt from eastern Australia (Phillips and Hughes 1996; Peters et al 1990); the Alaska–Juneau, Treadwell, Kensington mines in the Juneau gold belt in the North American Cordillera (Goldfarb et al. 1991; Miller et al. 1995), the Omchak goldfield in the Yana-Kolyma belt in northeastern Russia (Nokleberg et al. 1994;

102 Nokleberg et al. 1996), and the Reefton goldfield in eastern New Zealand (Cooper and
103 Tulloch 1992; Goldfarb et al. 1995).

104   The sedimentary rock-hosted lode gold deposits in eastern Australia are
105 similar in some aspects to the Klipwal gold deposit described here. Gold-bearing
106 quartz veins in the Hodgkinson gold field, Queensland Australia, are found in low-
107 grade metasediments with restricted hydrothermal alteration halos. Mineralization is
108 concentrated in brittle to brittle-ductile shear zones that occur within reactivated
109 second-generation fold axial planes (Peters et al. 1990). Geological characteristics,
110 isotopic data, alteration mineralogy, and fluid inclusion studies show that upward
111 migrating homogeneous metamorphic or distal magmatic fluids were responsible for
112 the gold mineralization (Peters et al. 1990). The Ballarat East gold field is located in
113 close proximity to the Avoca fault (Fairmaid et al. 2011) with gold hosted in large
114 fault-related quartz veins that are stacked in arrays associated with west-dipping
115 reverse faults. Evidence of mixing metamorphogenic fluid with sedimentary
116 formation waters is documented by Fairmaid et al. (2011). The sources of gold are
117 considered to include the underlying Cambrian volcanic rocks, surrounding Paleozoic
118 sediments and Proterozoic continental crust.

119   In South Africa, the Mesoarchaean volcano-sedimentary sequence of the
120 Pongola Supergroup, exposed in the southeastern part of the Kaapvaal craton (Fig.
121 1a), is considered contemporaneous with the Witwatersrand Supergroup and similarly
122 contains paleo-placer Au-U conglomerate occurrences (Bullen et al. 1994). In
123 addition to Witwatersrand type paleo-placer deposits, the Pongola Supergroup hosts a
124 number of epigenetic, structurally controlled orogenic-style lode gold deposits (Fig.
125 1b). These include the Wonder Mine situated in the Bumbeni Shear Zone, the Klipwal
126 Gold Mine (KGM) on the Klipwal Shear Zone (KSZ) and Ngotshe Mine located a
127 few hundred meters east of the KSZ (Bullen et al. 1994). As opposed to the Pongola
128 paleo-placer deposits the lode gold deposits have until recently continuously produced
129 gold, especially from the Klipwal Gold Mine (Bullen et al. 1994; Gold 1993; Gold
130 2006). Presently the mine is not in operation.

131   Here we present a detailed description of the geology of the Klipwal gold
132 deposit, its alteration mineralogy, P-T conditions of mineralization deduced from
133 chlorite and arsenopyrite geothermometry and fluid inclusion studies on mineralized
134 zones (reefs). In addition, we present Re-Os compositions of pyrite and arsenopyrite
135 from the ore and report on the timing of gold mineralization. The Klipwal Gold Mine

4

136   (KGM) is located in KwaZulu-Natal Province of South Africa, about 15 km south of

137   the Swaziland border, between the towns of Piet Retief and Pongola (Figs. 1a, b).

138   Mining operations commenced during the late nineteenth century with a total gold

139   production of 5.7 tons by 2003. A total of 1.18 million tons of ore were mined

140   between 1981 and 2003, and from these, at least 5.3 tons of gold were recovered at a

141   grade of 4.5 g/t. Mining operations extended fifteen levels to a depth of 454 m. This

142   study is based mainly on samples collected from levels six through to ten.

143

144   **Regional geological setting**

145

146   The Pongola Supergroup is preserved as two structural basins, the extensive Pongola

147   basin in the north and the smaller Nkandla basin in the south, separated by the

148   Babanango structural high within a stabilized segment of the southeastern Kaapvaal

149   craton (Matthews 1990; Gold 1993; Gold and Von Veh 1995; Gold 2006). The basins

150   comprise a lower volcano-sedimentary sequence, the Nsuze Group and an upper

151   dominantly sedimentary sequence, the Mozaan Group. The Nsuze Group is

152   characterized by 4.6 km of mafic and subordinate felsic volcanic rocks with minor

153   calcareous and siliciclastic sedimentary units. The overlying Mozaan Group, with a

154   maximum thickness of 5 km, comprises arenaceous and iron-rich argillaceous

155   sediments with minor banded ironstones. The Mozaan Group hosts both the placer

156   and lode gold deposits, with the KSZ the most important, displacing interbedded

157   sandstone, mudstone, ferruginous siltstone and two diamictite units of the Delfkom

158   Formation of the Odwaleni Subgroup (Fig. 1c).

159

160   Structure

161

162   The Pongola Supergroup in the central and main Pongola basin is gently deformed

163   and typically metamorphosed under sub-greenschist to greenschist facies conditions,

164   with the exception of high-grade occurrences in Swaziland where granulite facies

165   conditions had been reached locally (Wilson and Jackson 1988; Gold and Von Veh

166   1995; Saggerson and Turner 1995, Mukasa et al. 2013; Horvath et al. 2014). Gold and

167   Von Veh (1995) in accordance with Matthews (1990) proposed three regional

168   deformational events (D_1, D_2 and D_3) affecting the main Pongola basin (Fig. 1). D_1 is

169   represented by early NNW-directed thrusts, reverse faults and shear zones, including

170   the KSZ (Fig. 1). During D_1, ENE-trending F_1 folds developed contemporaneously

171   with NNW-directed thrusting. Following D_1 compressional tectonics, the area was

172   affected by NW-SE extension (D_2) associated with the emplacement of mafic dykes

173   and sills. This was followed by D_3 NE-SW-directed compression which produced

174   major northwesterly trending, open upright F_3 folds that deformed the early D_1 shears

175   and refolded the ENE-trending F_1 folds forming a dome-and-basin interference

176   pattern (Gold and Von Veh 1995). Between D_2 and D_3 a number of granitoid plutons

177   intruded into the Pongola Supergroup, collectively known as the post-Pongola

178   granites (Gold 2006).

179   The KSZ is interpreted by Gold (2006) as a D_1 structure. It forms a major

180   shear zone extending approximately N-S for about 20 km, characterized by a

181   moderately dipping brittle-ductile shear plane that displays oblique-reverse sinistral

182   sense of shear. The shear zone shows anastomosing shear fabrics with numerous

183   shear-parallel laminated quartz-carbonate veins and, in places, a quartz-vein

184   stockwork. There is also evidence of late brittle reactivation of the shear plane (Gold

185   2006).

186

187   Geochronology of granitoids

188

189   The ages of deformation and low-grade regional metamorphism remain poorly

190   constrained due to the lack of reliable age data, whereas the geochronology of

191   basement rocks to the Pongola Supergroup and the post-Pongola granites is well

192   established. The basement granitoid rocks of the Anhalt granitoid suite intruded into

193   3300 Ma old greenstone remnants (such as the Nondweni greenstone fragment) in the

194   southeastern Kaapvaal craton (Farrow et al. 1990; Hunter et al. 1992; Robb et al.

195   2006). These granitoids range in age from 3290 to 3028 Ma (Rb-Sr: Barton et al.

196   1983; Farrow et al. 1990; Matthews et al. 1989; U-Pb: Kamo and Davis 1994). The

197   pre-Pongola Tsawela gneiss on the northern side of the Pongola basin formed at

198   3428±22 Ma (U-Pb single zircon: Mukasa et al. 2013). The Nsuze Group volcanic

199   rocks, which non-conformably overlie the basement, were erupted between 2984±3

200   Ma (U-Pb single zircon: Hegner et al. 1993) and 2940±22 Ma (U-Pb: Hegner et al.

201   1984). On the basis of new U-Pb zircon age data, Mukasa et al. (2013) established the

202   period of deposition for the Pongola sequence rocks. Accordingly, the oldest Nsuze

203   group volcanic layers date at 2980± 10 Ma, which is similar to the previously

6

published ages, and the uppermost sedimentary layers of the Mozaan group have an age of 2954±9 Ma. The post-Pongola granitoids (cf. Fig. 1b) were emplaced over a period of about 150 Ma, between 2863 and 2721 Ma. The Godlwayo granite has been dated at 2863±8 Ma (Reimold et al. 1993), the Nzimane granite in the Hlabisa area at 2739±3 Ma (Thomas et al. 1995) and the Spekboom granite at 2700–2730 Ma (Reimold et al. 1993). Maphalala and Kröner (1993) obtained an age of 2722 ± 6 Ma for the Kwetta Granite. All these ages were obtained from single zircon Pb-evaporation method. Mukasa et al. (2013) constrained the emplacement ages for Kwetta and Mswati granites, using U-Pb zircon studies, at 2721± 10 Ma and 2723±7 Ma respectively.

Geology of the Klipwal Gold Mine

Wall rocks, structures and distribution of the reefs

The Klipwal Shear Zone cuts the Delfkom Formation of the upper Mozaan Group which comprises interbedded sandstone, siltstone, mudstone, diamictite and associated mafic and ultramafic intrusives, possibly related to the ca. 2.8 Ga Usushwana intrusive event. Gold mineralization at the KGM is centered on a convex-westward flexure in the KSZ (Fig. 1c). At least three closely spaced economic reefs are developed (Fig. 2a). The main R-reef constitutes the master shear zone while the J- and H- reefs are lodes that occupy footwall splays of varying dip. The fourth Quartz (Q)- reef is less extensive and developed as a footwall splay of the R-reef in the upper levels (Fig. 2a). The Q-reef and a major portion of the R-reef are mostly mined out. The R-reef is a curvy-planar structure dipping steeply (about 70°) in the upper levels, while gradually changing to a gentle dip at deeper levels, to as little as 35°. The most pervasive fabric observed within the KSZ is an N-S trending shear foliation which is best observed underground as it is poorly exposed on the surface. The observed structures constitute an early-formed set indicating compression, which includes the main shear zone, its mylonitic wall rocks, fault-fill veins and sub-horizontal extensional veins. A late phase of brittle faulting of the extensional veins produced a fault breccia. Poles to the major shear foliation show a point maximum corresponding to a mean strike of 014° and a dip angle of 50°E. The bulk of the variation in shear foliation orientation is within a dip direction interval from about E to ESE, and a dip

238 angle range between shallow and moderately steep angles. Some deviation of the
239 shallow-dipping sections to more southerly dips and a corresponding clockwise
240 rotation of the strike are evident in the plot of Figure 2b. The relatively well-defined
241 pole maximum in Figure 2b, however, partly reflects a bias in the readings being
242 taken at underground levels accessible for this study. This effectively reduces the
243 spread of the dip and strike data expected over the entire fault structure.

244 Old mine excavations of the Q-reef at the surface show that the footwall
245 comprises altered siltstone (quartz–chlorite–carbonate±muscovite–schist) and
246 sandstone (metapsammite) in the hanging wall (Fig. 3a). Henceforth, these two rocks
247 are named chlorite-carbonate schist and metapsammite, respectively. Although the
248 shear fabric is not often observed on surface, reactivation of the shear plane is evident
249 from slickensides (Fig. 3b). Shear-related folds, with a NW trending axial planar
250 fabric, are observed in the siltstone (Fig. 3c). Strongly foliated sandstone occurs in
251 close proximity to the shear zone (Fig. 3d).

252 The R-reef comprises a 0.5–5.5 m wide, strongly foliated zone, containing
253 numerous shear-parallel fault-fill laminated quartz veins that range in thickness from
254 less than 1 cm to a few meters (Fig. 4a). The N-S trending foliation in the R-reef
255 forms mylonitic fabrics and locally preserves S-C fabrics indicating a horizontal offset
256 with a sinistral sense of shear (Figs. 4a, b). Shear lenses comprising smoky quartz
257 grains are observed in the mylonites (Fig. 4b). In places, an array of thin subhorizontal
258 extensional veins are observed in the R-reef (Fig. 4c). The contact between the R-reef
259 and its hanging-wall shows evidence of late brittle reactivation indicated by clay-rich
260 fault gouge and/or breccia (Fig. 4d). The fault breccia consists of fragments of fault-
261 fill quartz veins as well as country rocks. Sub-horizontal extensional veins are
262 displaced by the later brittle faults (Fig. 4e).

263 The H-reefs form a number of footwall splays that developed from the R-reef,
264 linking across to a sequence of reefs known as the J-reefs (Fig. 2a). The H-reefs are
265 similar to the R-reef in that they are also characterized by brittle-ductile shears, but
266 were not reactivated to the same extent during later brittle faulting. The fabric in the
267 quartz veins is less pervasive, and fault breccia is absent (Fig. 4f). A crosscut at level
268 10 (~350m from shaft surface) from the main R-reef, provided an opportunity to
269 access the H- and J-reef shear zones and quartz veins underground (Fig. 5). These
270 reefs cut across a range of footwall lithologies such as metapsammite, least-altered

271   sandstone and chlorite-carbonate schist that strike sub-parallel to, and dip at shallower

272   angles than, the R-reef (Fig. 5).

273   J-reefs represent footwall mineralization of the H-reef shears (Hilliard 2007)

274   where the H-reef shears cut and displace the contact between least-altered sandstone

275   and chlorite–carbonate schist (Figs. 2a and 5). J-reef ores typically extend for a

276   distance of between 10 and 50 m representing the amount of displacement along the

277   H-reef. Juxtaposition of the sandstone against siltstone along the H-reef shears is

278   considered a critical controlling factor in J-reef development.

279

280   **Alteration mineralogy**

281

282   Petrographic studies reveal an inner and a proximal alteration zones centered on the

283   KSZ. The inner zone is dominated by laminated quartz-carbonate veins with

284   alternating quartz-carbonate and muscovite-chlorite-rich layers. The proximal zone is

285   characterized by an alteration halo of K-feldspar, albite and chlorite, along with

286   carbonate and associated quartz veins surrounding the inner zone.

287   About 30 m away from the KSZ, in the upper level, sandstone in the least

288   altered zone comprises quartz grains with less K-feldspar, plagioclase, muscovite

289   (Fig. 6a) and minor heavy minerals such as zircon, ilmenite and titanite. The clastic

290   components are cemented by quartz. K-feldspar and plagioclase are unaltered (Fig.

291   6a). A weak S_1 foliation is defined by muscovite (Fig. 6a) that is considered to have

292   formed during the development of the KSZ. Siltstone in the least altered zone is

293   characteristically weakly foliated with the schistosity being defined by chlorite and

294   muscovite (Fig. 6b).

295   In the proximal zone the altered metapsammite consists of microcline,

296   dolomite and magnesite, indicating potassic and carbonate alteration (Figs. 6c, d).

297   Minor chlorite and quartz are also observed in the rock as alteration products, and

298   albitic plagioclase is intensely altered to muscovite (Fig. 6d). Chlorite–carbonate

299   schist in the proximal zone is derived from hydrothermal alteration and deformation

300   of siltstone along the shear zone, producing a strong fabric defined by chlorite and

301   muscovite (Figs. 6e, f). Other minerals in this rock include epidote and quartz.

302   The inner alteration zone comprises auriferous laminated quartz-carbonate veins.

303   Alternating laminae in these veins consist predominantly of quartz-carbonate and

304   muscovite-chlorite (Fig. 7a). Carbonates in the veins include dolomite, magnesite and

siderite. A sinistral sense of shear is observed at thin-section scale with the development of an S−C fabric in the muscovite-chlorite lamina (Fig. 7b). The fine-grained texture and strong foliation indicate that the rocks experienced mylonitization and dynamic recrystallization in the shear zone. Matrix quartz grains display bulging and recrystallized grain boundaries, with some grains displaying subgrain rotation and formation of core-and-mantle structures (Figs. 7a, b, c). These textures indicate plastic deformation at low temperatures (about 300°C; Stipp et al. 2002) and correspond to sub-greenschist facies conditions. Shear lenses consisting of quartz grains are observed in the mylonitic matrix (Fig. 7d). Broken fragments of quartz vein clasts and mylonitic clasts are very well preserved in the fault breccia (Fig. 7e). Antitaxial quartz "strain fringes" within the mylonites (Fig. 7f, g) grew on rigid pyrite and arsenopyrite grains. In addition to quartz, these strain fringes sometimes contain chlorite. The 'jigsaw-puzzle' type brittle fractures in the sulfide grains are evident of hydraulic breccia and these fractures are filled with quartz and chlorite (Fig. 7f). Silicate inclusion trails within sulfides occur parallel to the matrix shear foliation (Fig. 7g, h) which suggest that either sulfides overgrowing an existing, unmodified early S_1 foliation in the D_3 event, or on a reactivated S_1-S_3 foliation, potentially during D_3. In both cases, the sulfide growth is associated with syn-D_3. As D_3 is a reactivation, presumably makes small angle between S_1 and S_3, it is difficult to distinguish these two fabrics.

Analytical techniques

Selected thin sections were analyzed for chlorite compositions using the CAMECA SX-100 electron probe micro-analyzer (EPMA) at the DST-EPMA National facility, Department of Geology and Geophysics, IIT Kharagpur. Operating conditions for chlorite analysis were 15 kV acceleration voltages with 20 nA beam currents. The counting time was 20 to 30 s. The beam diameter was set at 1 μm. For analysis of pyrite and arsenopyrite an acceleration potential of 20 kV was used. Beam currents of 200 nA and 20 nA for was used for pyrite and arsenopyrite respectively. The counting time for Fe and S was 20s and for As 40s.-Appropriate natural and synthetic minerals were used for standardization. Raw data were corrected with the help of PAP correction program by Pouchou and Pichoir (1984). Back scattered electron (BSE)

imaging was acquired using JEOL JSM 6490 SEM at the Department of Geology and Geophysics, IIT Kharagpur.

Nine doubly polished wafers of ~200 μm thickness were prepared for fluid inclusion petrographic study. Microthermometric runs were conducted on five samples with the help of a Fluid Inc. adapted USGS gas flow microscopic heating-freezing stage, fitted on a Leica Laborlux D petrological microscope housed at Geological Sciences, University of Kwazulu-Natal, Durban. The unit operates in the temperature range of −195 °C to 700 °C, and is periodically calibrated using distilled water-ice bath (0 °C) and pure CO_2 inclusions (−56.6 °C). Phase changes were observed during heating. Fluid salinity and density values were calculated and isochores were constructed using the FLUIDS software package (Bakker 2003). For type-I inclusions the DENSITY program in package CLATHRATES (Bakker 1997) was used. Equation of state (EOS) of Duan et al. (1992a, b) and Bakker (1999) was used for salinity and density calculation and isochore construction respectively. For type-II inclusions, EOS of Jacobs and Kerrich (1980) was used for calculating density, and for isochore construction Belonoshko and Saxena (1991) was used. For type-III inclusions Thiéry et al. (1994) and Duan et al (1992a) were used for calculation of density and isochore respectively. For type-IV inclusions Bodnar (1993) was used to calculate salinity and Zhang and Frants (1987) for density. A Renishaw RM1000B laser Raman probe, attached to a Leica microscope, at the Department of Geology and Geophysics, IIT Kharagpur was used to analyze fluid inclusions. The system is equipped with edge filters to block the Rayleigh lines, confocal configuration, thermoelectrically cooled CCD detector, air-cooled laser, and associated software to acquire and evaluate the spectral data. Irradiation was by the 514.5 nm line of a continuous wave Ar-ion laser, which delivered ~ 8 mW laser power at the sample surface. The acquisition time was 60 seconds. The first order Raman band of silicon at 520 cm^{-1} was used for routine calibration. The reproducibility of the Raman wave number was set up to be ± 1 cm^{-1}. Equation (2) of Burke (2001) is used for quantitative analysis of gas species (X_{CO2} and X_{CH4}) from the respective peak areas. Raman results were also compared to the graphical methods of Thiéry et al. (1994). The observed maximum uncertainty in species composition is below 5% between these two methods.

For Re-Os analysis, sulfide minerals (pyrite and arsenopyrite) were prepared using traditional methods, crushing without metal contact, heavy liquids, FRANTZ

11

372 magnetic separation and hand picking. Re and Os abundance and isotope

373 compositions were determined using isotope dilution negative ion thermal mass

374 spectrometry (Selby et al. 2009). In brief, approximately ~400 mg of

375 pyrite/arsenopyrite were dissolved with a known amount of mixed tracer solution

376 (^{185}Re, ^{190}Os) in 8 ml of inverse *aqua regia* (1:3 mix of HCl and HNO$_3$) in a carius

377 tube at 220˚C for 48 hrs. Osmium was isolated and purified from the acid solution

378 using chloroform solvent extraction (CHCl$_3$) and micro-distillation methods. Rhenium

379 was isolated using solvent extraction (NaOH-acetone; Cumming et al. 2013) and

380 anion chromatography. Full procedural blanks were 0.1 ± 0.1 and 6.2 ± 5.4 ppt (1 SD;

381 n = 2) for Os and Re, respectively, with an ^{187}Os/^{188}Os of 0.25 ± 0.02.

382 The in-house solution standards (Re std; DROsS) analyzed during the period of these

383 are 0.59773 ± 0.002 and 0.16093 ± 0.0002 (n = 2), respectively, which are identical to

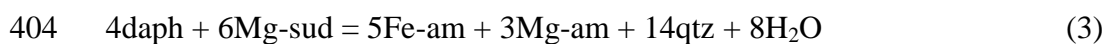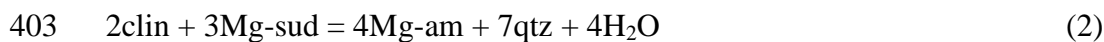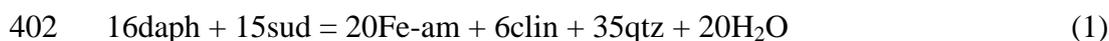384 those previously reported (Cumming et al. 2012 and references therein).

385

386 **Chlorite geothermometry**

387

388 Chlorite compositions have been used for temperature estimation and this was done

389 by: (1) empirical calibrations based on tetrahedral Al content and amount of

390 octahedral vacancy (Cathelineau and Nieva 1985; Zang and Fyfe 1995), and (2)

391 thermodynamic formulation, using intra-crystalline exchange reactions between the

392 chlorite phase components and their temperature-pressure dependence (Vidal et al.

393 2001; 2005). In the latter thermodynamic model four end members are considered:

394 clinochlore [Si$_3$Al$_2$Mg$_5$O$_{10}$(OH)$_8$], daphnite [Si$_3$Al$_2$Fe$_5$O$_{10}$(OH)$_8$], Mg-amesite

395 [Si$_2$Al$_4$Mg$_4$O$_{10}$(OH)$_8$] and sudoite [Si$_3$Al$_4$(Mg,Fe)$_2$□O$_{10}$(OH)$_8$]. These end members

396 are necessary to model the (i) tschermak (TK), (ii) Fe-Mg (FM), and (iii)

397 dioctahedral-trioctahedral (DT) substitutions in chlorite. Temperatures of chlorite

398 formation in alteration and ore zones (reefs) have been calculated from the equations

399 of state of three intra-crystalline equilibria (eqns. 1 through 3), at a pressure of 2 kbar.

400 The chosen pressure is justified from the fluid inclusion studies discussed below.

401

402 $16\text{daph} + 15\text{sud} = 20\text{Fe-am} + 6\text{clin} + 35\text{qtz} + 20\text{H}_2\text{O}$ (1)

403 $2\text{clin} + 3\text{Mg-sud} = 4\text{Mg-am} + 7\text{qtz} + 4\text{H}_2\text{O}$ (2)

404 $4\text{daph} + 6\text{Mg-sud} = 5\text{Fe-am} + 3\text{Mg-am} + 14\text{qtz} + 8\text{H}_2\text{O}$ (3)

405

406   Two samples each from the R- and J- reefs were selected for electron

407   microprobe analysis. Representative chlorite analyses, their structural formulae and

408   estimated temperatures are given in Table 1. Average temperatures, estimated using

409   the empirical calibrations fall in the range of 267–301°C. Similarly, average

410   temperatures, computed using reactions (1) through (3) are in the ranges of

411   268–312°C. Hence, both approaches furnished comparable temperatures, with

412   reasonable standard deviations. However, it should be noted that whenever the

413   estimated temperature values are high, the calculated X_{Fe}^{3+} values are too low. In

414   order to reduce the temperature, a_{H2O} is decreased to as low as 0.2. This is mainly

415   because a decrease of X_{Fe}^{3+} leads to a related decrease of octahedral Al and vacancy

416   with increase in octahedral summation, consequently leading to an increase in the

417   estimated temperature (Vidal et al. 2005; 2006). Similarly a decrease in a_{H2O} leads to

418   a decrease in the equilibrium constants of reactions (1) through (3) and therefore

419   decreases the estimated temperature. A decrease in fluid content in the rock suggest

420   periods of reduced fluid flow due to closure of the fractures during interseismic stage

421   (Sibson, 2001). In the present case, reduced a_{H2O} values were used to make the

422   temperatures compatible with those obtained by empirical calibrations.

423

424   **Ore mineralogy**

425

426   In the inner zone, the dominant sulfide minerals are, in decreasing order of

427   abundance, pyrite and arsenopyrite, with minor chalcopyrite, pyrrhotite and galena. In

428   the proximal zone pyrite, arsenopyrite, chalcopyrite, pyrrhotite, and sphalerite occur.

429   Ilmenite, rutile, and titanite occur in both zones. Ore mineral aggregates are aligned

430   along the sheared and mylonitized fabric. Texturally, three types of pyrite and two

431   types of arsenopyrite are present (Figs. 8a and 9). Pyrite-I ranges in size between

432   100μm and >1mm. It forms porphyroblasts with the shear foliation wrapping around

433   them (Figs. 7g, h, 8a and 9). Euhedral grains of pyrite-I contain numerous randomly

434   to preferentially oriented silicate inclusions mimic matrix foliation (Figs. 7g, h and

435   8b). Sulfides such as chalcopyrite, pyrrhotite and galena and gold also occur as

436   inclusions (Figs. 8c, d). Pyrite-II, which overgrew pyrite-I, has also euhedral grain

437   boundaries and is almost free of silicate inclusions (Figs. 8a, d) but contains

438   inclusions of other sulfides such as chalcopyrite, arsenopyrite-II and pyrrhotite (Fig.

13

8d). Pyrite-III has a characteristic irregular outline with or without silicate inclusions and occurs as elongated grains aligned either along the shear foliation or overgrowing this deformation fabric (Fig. 8a). Pyrite-I contains up to 2.8 wt % As and may be referred to as arsenian pyrite (cf. Large et al. 2009). SEM-back scattered electron (BSE) images show that these pyrites are weakly zoned with respect to As showing As-poor cores (Fig. 8e). Pyrite-II shows concentric As-rich and As-poor zones (Figs. 8f, g) but also irregular As zoning patterns (Fig. 8h). Arsenopyrite-I is represented by large euhedral grains with abundant randomly oriented silicate inclusions and may contain inclusions of pyrite-II (Fig. 8b). Arsenopyrite-II is euhedral to subhedral in shape, smaller in size and free of any silicate inclusions (Figs. 8c, d). Arsenopyrite-II in places overgrows pyrite-I (Fig. 8c). Gold occurs mostly in association with sulfides and occasionally as free gold grains in quartz veins. Gold grains are generally 10–20 μm in size and occasionally as large as 100 μm. Gold occurs as

(1) inclusions within pyrite-I, at the interface with other sulfides like chalcopyrite with pyrite (Fig. 10a),

(2) inclusions within pyrite-I without other sulfide inclusions (Fig. 10b),

(3) inclusions within arsenopyrite-II (Fig. 10c), and

(4) free gold in the silicate matrix in close proximity to sulfides and chlorite (Fig. 10d).

Arsenopyrite geothermometry

As described earlier, arsenopyrite- I and II occur in association with pyrite in the proximal and inner alteration zones. The temperature of formation can be inferred from arsenic contents of arsenopyrite as described in Kretschmar and Scott (1976) and Sharp et al. (1985). In selected samples (KU10A and KU16) arsenopyrite grains were analyzed by electron microprobe. Representative analytical data and the deduced temperatures are summarized in Table 2. In sulfur rich assemblage (arsenopyrite with pyrite and/or pyrrhotite) arsenopyrite may contain less than 30 atomic % arsenic due to non-equilibrium feature reflecting the kinetics of growth of arsenopyrite and local fluctuations in f_{S2}/f_{As2} (Kretschmar and Scott 1976). Temperature values were inferred up to ~28.4 atomic % arsenic. The estimated temperatures vary from 255 °C to 318°C, while the corresponding $\log f_{S2}$ falls in the range of –9.9 to –12, comparing well to the temperatures obtained from chlorite geothermometry.

473

Fluid inclusion studies

475

Fluid inclusion studies, involving inclusion petrography, microthermometry and Raman spectroscopy in quartz veins from all reefs were carried out. A total of nine doubly polished wafer sections were prepared for examination and five samples (two from R- and J-reefs and one sample from H-reef) were selected for microthermometry. The choice of these samples was based on the availability of workable inclusions within suitable Group of Synchronous Inclusions (GSI, cf. Touret 2001). Grains that showed indications of dynamic recrystallization and inclusions showing stretching or leakage were carefully avoided.

Inclusions are generally small in size ranging from less than 2 μm to 10 μm. Inclusions occurring as isolated, clustered and as intra-granular trails were considered as primary and pseudo secondary, respectively, and selected for microthermometric runs. Inclusions were classified on the basis of disposition and phase content in ambient laboratory conditions, and grouped into four types. Type-I aqueous gaseous inclusions contain a dark gas-rich bubble surrounded by aqueous liquid (Fig. 11a). The volume percent of gaseous phase varies from 40 to 90 % (Table 3). At times inclusion walls are decrepitated due to high internal pressure while heating the inclusions. Type-II and type-III inclusions are monophase gaseous inclusions in which type-II inclusions exclusively contain pure methane as a gas phase (Figs. 11b, c). Type-III inclusions contain a gas mixture of CO_2 and CH_4 with varying proportions (X_{CH4} up to 0.31; Table 3) (Figs. 11b, d). Type-IV inclusions are low salinity aqueous biphase inclusions (Fig. 11e) that frequently occur within the same clusters as type-II and III inclusions (Fig. 11f) and in places they also occur as intra-granular trails. Vapor occupies 10 to 20 % of volume in type-IV inclusions.

For type-I inclusions complete microthermometry data could be obtained on only 21 inclusions (12 from R-reef and 9 from J-reef; Table 3). The temperature of CO_2 melting ($T_{m,CO2}$) varies from -57.8 to -63.2 °C and the temperature of CO_2 vapor homogenization ($T_{h,CO2}$) varies from -15.5 to +7.8 °C. Clathrate melting ($T_{m,Cl}$) varies from +7.8 to +14.8 C. Temperature of total homogenization ($T_{h,tot}$) varies from 272 to 367 °C. For some of the inclusions decrepitation temperatures were recorded and the final homogenization was into a gaseous phase. The temperature of CH_4 vapor homogenization ($T_{h,CH4}$) for type-II inclusions varies from -94.3 to -84.3 °C (Fig.

15

507 12a). The temperature of CH_4 melting ($T_{m,CH4}$) could not be measured because the

508 stage only cools to -196 °C using liquid nitrogen as cooling agent. For type-III

509 inclusions the observed variation in $T_{m,CO2}$: was -63.9 to -56.6 °C (Fig.12b). $T_{h,CO2}$

510 varied from -20.1 to +18.3 °C (Fig.12c). From Raman spectrometric analyses CH_4

511 (Fig. 11d) is the only gas identified in these inclusions apart from CO_2. For type-IV

512 inclusions temperatures of last ice melting ($T_{m,ice}$) varied from -16.1 to +0.2 °C (Fig.

513 12d) and final liquid vapor homogenization ($T_{h,tot}$) was into liquid phase with values

514 ranged from 115 to 302 °C (Fig. 12e).

515   The average calculated salinity for type-IV inclusions is 6.5±4.3 (wt% NaCl

516 equiv.). The isochore intersection geobarometric method described by Roedder and

517 Bodnar (1980) was adopted to estimate the entrapment P-T conditions of the

518 inclusions. Coexisting carbonic (type-III) and aqueous (type-IV) inclusions occurring

519 in the same GSI are considered as coeval inclusions (Fig. 11f). The assumption is that

520 these inclusions were entrapped simultaneously and no post-entrapment modifications

521 of the inclusions had taken place. Two intersection points, from the isochores of these

522 inclusion types, IS-1 (275 °C and 1.8 kbar) and IS-2 (287 °C and 1.5 kbar) furnished

523 P-T values (Fig 13). In addition, pressure values were further inferred from the

524 intersection of the isochores with chlorite (CT) and arsenopyrite (AT)

525 geothermometry (Fig 13). This intersection additionally furnished a pressure range of

526 1.1 to 2.5 kbar with the thermometry by the two above independent approaches

527 yielding comparable P-T values. This further supports the use of the isochore

528 intersection method.

529

530 **Re–Os geochronology**

531

532 Two samples from each of the three mineralized reefs were selected for Re-Os

533 analysis to determine the age of sulfide and gold mineralization. The samples were

534 collected from the fault-fill laminated quartz veins in the inner zone that contains a

535 profuse amount of sulfides in very close association with the gold mineralization. The

536 Re-Os data for the six samples are presented in Table 4. The pyrite and arsenopyrite

537 grains contain between ~0.2 and 4.7 ppb Re and 32 and 240 ppt Os. A significant

538 portion of the Os budget comprises ^{192}Os (7.7 to 45 ppt). The $^{187}Re/^{188}Os$ values are

539 low and range from ~19 to 210. These values positively correlate with the $^{187}Os/^{188}Os$

540 from ~1.11 to 9.44. Regression of the Re-Os data including rho using isoplot v. 4.15

541   (Ludwig, 1980) and the ^{187}Re decay (1.666 e^{-11} a^{-1}; Smoliar et al. 1996) yield a Model

542   1 Re-Os age of 2563 ± 84 Ma (MSWD = 0.38), with a relatively unradiogenic initial

543   ^{187}Os/^{188}Os value of 0.29 ± 0.08 (Fig. 14).

544

545   **Discussion and conclusions**

546

547   Regional and mine scale structures

548

549   Although three regional-scale deformation events (D$_1$, D$_2$, and D$_3$) have been

550   described (Gold and Von Veh 1995 and Gold 2006), only an earlier set of ductile-

551   brittle structures and a final brittle deformation are recognized in the mine. Since

552   mineralization postdates the emplacement of the post-Pongola granites which

553   occurred between D$_2$ and D$_3$, the initial development of the shear zone is considered

554   to have developed during D$_1$ with mineralization occurring during D$_3$ involving

555   folding and shear zone reactivation. D$_1$ generated the initial KSZ geometry (R-reef)

556   and footwall splay (H-reef) during NNW-oriented thrusting. The D$_2$ event, which is

557   regionally related to the emplacement of mafic dykes and sills and which was

558   followed by the emplacement of the post-Pongola granites, is not recognized in the

559   mine as forming any distinct meso- or microscale structures.

560   The area south-west of Swaziland, where the Mozaan Group is most

561   extensively developed and which includes the Klipwal mine, is characterized by the

562   lowest-grade metamorphic imprint of all the exposed Pongola Supergroup. This

563   region was classified as "unmetamorphosed" by Saggerson and Turner (1995),

564   although it should more appropriately be referred to as "very-low grade metamorphic"

565   with no evidence that regional metamorphism ever exceeded lowermost greenschist

566   facies during any of the deformational events. If the original KSZ formed during D$_1$,

567   under very-low grade metamorphic conditions, the subsequent reactivation of

568   structures and mineralization during the regional D$_3$ event occurred under similar

569   temperature conditions, making the two events difficult to distinguish. Nevertheless,

570   microstructural evidence confirms post-D$_1$ ductile deformation. As sulfide growth

571   generally postdates the early-formed (D$_1$) shear zone, the sulfides can be used as

572   microstructural markers with respect to ductile overprinting of D$_1$ structures during

573   D$_3$. Critical evidence includes the preservation of an early-formed foliation as

574   inclusion trails within sulfides, and sulfide-matrix relationships (strain fringes,

17

575   foliation wrapping around sulfides, while late-formed sufides overgrew the foliation;

576   Figs. 7g, h, 8a and 9). Thus, the period of sulfide growth overlaps to a large extent

577   with D_3 deformation.

578   The thermobarometric data extracted from the mineralized rocks, as well as

579   the related structures, are considered to represent the metamorphic-structural D_3

580   overprint as supported by the consistency of the data between silicate equilibria and

581   sulfides. Mineralization was related to a substantial influx of fluids during D_3. Fluid

582   pathways exploited the D_3-modified and reactivated KSZ and its related vein systems

583   as well as lithological contacts, becoming sites of sulfide-gold precipitation. The

584   actual origin of the mineralizing fluid remains to be discussed, but late fluid

585   infiltration can be recognized on a regional scale. Saggerson and Turner (1995) note

586   that post-peak hydrous alteration of metamorphic mineral assemblages is widespread

587   in the Pongola Supergroup. The final (post-D_3) brittle effects on the shear zone

588   produced fault breccia comprising fragments of quartz veins, mineralized domains

589   and mylonitic wall rocks (Fig. 4d). This event is most likely part of the regional Karoo

590   extensional faulting related to the breakup of Gondwana.

591   The J-reef with higher gold grades was developed at the contact between

592   metapsammite and chlorite-carbonate schist (Figs. 2a and 5). Hence the original

593   lithological discontinuity provided a fluid conduit for J-reef mineralization. On the

594   regional scale, the KSZ strikes approximately N–S. However, at the KGM there is a

595   change in direction from the N–S to a NNE–SSW orientation (Fig.1c). This change in

596   the shear zone geometry, is considered to be a result of the regional D_3 folding event

597   which produced a convex westward flexure in the KSZ and generated a

598   'compressional jog' through which regional fluid flow was driven (cf. Cox et al. 2001;

599   Sibson, 2001).

600   The shear zone contains profuse laminated quartz veins that are developed as

601   fault-fill veins (Fig 4a) due to formation of microfractures along the shear planes.

602   Microfracturing, along grain boundaries, is the dominant mechanism for the formation

603   of grain scale porosities in the ductile regime (Knipe and McCaig 1994; McCaig

604   1997; Mancktelow et al. 1998; Kolb et al. 2004). These microfractures generate

605   fracture porosity and increase fluid permeability along the shear zone (Cox et al.

606   2001), increasing pervasive fluid flow through the shear zone. Fractures provided the

607   open space for rapid flow of the gold-bearing ore fluids. The 'jigsaw-puzzle' type

608   brittle fracturing with angular fragments observed in sulfide grains (Fig. 8f) are

609 interpreted to represent hydraulic breccias which point to hydraulic fracturing, as a

610 mechanism for fracture formation, as described by Robert et al. (1995); Kisters et al.

611 (2000) and Kolb et al. (2004).

612

613 Extensional veins and pressure fluctuation

614

615 Oblique or sub-horizontal extensional vein arrays are also observed in association

616 with the shear zone and fault-fill veins (Fig. 4c). These veins represent hydraulic

617 extension fractures, which opened during vein filling episodes by fluid pressures (P_f)

618 in excess of the lithostatic pressure (i.e., $P_f \geq \sigma_3 + T$, where T = tensile strength of the

619 rock) (Robert and Brown 1986). Extensional fractures typically develop parallel to σ_1

620 when σ_3' ($\sigma_3' = \sigma_3 - P_f$) equals or exceeds the tensile strength of the rock. This

621 situation is only possible under conditions of low differential stress. Hence,

622 extensional fracturing (possible at negative values of σ_3') can only be attainable by

623 elevated fluid pressure in the inferred compressional environments of formation of

624 orogenic gold deposits (Sibson et al. 1988; Sibson 2001; Robert and Poulsen 2001).

625 Kolb et al. (2004) demonstrated the effect of change in shear zone geometry

626 for economic gold mineralization in the world class Hutti gold mine in the Hutti-

627 Muski greenstone belt, eastern Dharwar craton, India. Mishra and Pal (2008) reported

628 oblique sigmoidal extensional veins, similar to the subhorizontal extensional veins in

629 the KSZ in the Hira-Buddini mine from the same Hutti-Muski greenstone belt. These

630 veins were formed by hydraulic fracturing during brittle-ductile shearing. At the Val

631 d'Or lode gold deposits at Quebec Canada, Bouillier and Robert (1992) established

632 that successive cycles of opening and collapse in subhorizontal extension veins

633 correlated with opening and slip on high-angle shear veins. They interpreted these

634 observations to be a result of fluid pressure fluctuations in successive coseismic-

635 interseismic cycles (McCuig and Kerrich 1998). Formation of laminated quartz veins

636 requires episodes in which fluid pressure exceeds the local normal stress on the fault.

637 Hence, a crack-seal and/or a fault valve mechanism are interpreted to have operated at

638 KGM during the mineralization event producing the laminated veins.

639 Fluid inclusion density variation further supports pressure fluctuation during

640 gold mineralization. The wide distribution in $T_{h,CO2}$ values of Type-III inclusions

641 indicates a significant variation in density (Table 3), which is attributed to fluctuation

642 in fluid composition and/or pressure. In order to determine the exclusive effect of

19

643   pressure, $T_{m,CO2}$–$T_{h,CO2}$ plots (Fig. 12f) were prepared for inclusions with maximum

644   lowering in $T_{m,CO2}$ up to −57 °C, i.e., pure CO_2. The plot shows significant variation

645   of $T_{h,CO2}$ for a near-constant $T_{m,CO2}$, implying fluid pressure fluctuations at the time of

646   entrapment (cf. Dugdale and Hagemann, 2001).

647   Crystal plastic deformation microstructures are observed in the quartz grains

648   but are absent in feldspar grains, which suggests that the deformation occurred at

649   greenschist facies conditions (Scholz, 1988). Dynamic recrystallization structures of

650   quartz grains shows bulged and recrystallized grain boundaries, subgrain rotation and

651   core-mantle structures indicative of pressure solution and intracrystalline plastic

652   deformation at temperatures of about 300°C (Stipp et al. 2002). The alteration mineral

653   assemblage consisting of chlorite-muscovite-carbonates±epidote-quartz-pyrite-

654   arsenopyrite surrounding the shear zone in the host rocks is characteristic of low to

655   sub-greenschist facies conditions. Estimates from fluid inclusion isochore

656   intersections coupled with the chlorite and arsenopyrite thermometry (Fig. 13) further

657   confirm that the P-T conditions (255−318°C and 1.1 to 2.5 kbar) were at sub-

658   greenschist facies. These temperatures and the observed alteration mineralogy in the

659   proximal and inner zone are consistent with the typical mesozonal orogenic gold

660   deposits elsewhere (McCuaig and Kerrich 1998; Groves et al. 1998; Goldfarb et al.

661   2001; Groves et al. 2003; Elmer et al. 2006).

662

663   Ore fluid composition

664

665   Irrespective of the host rock, metamorphism and age, the observed fluid composition

666   in orogenic gold deposits shows a very narrow range which is in general aqueous-

667   gaseous, low saline metamorphic and/or distant magmatic (Mikcuki 1998; McCuiag

668   and Kerrich 1998). For the Klipwal deposit, fluid inclusion studies reveal that the

669   original mineralizing fluid composition is H_2O-CO_2-CH_4-low salinity (~6 wt.% NaCl

670   equiv.). This is comparable with orogenic gold deposits around the world (Table 5) in

671   general, and sedimentary rock-hosted, Phanerozoic counter-parts in the Pacific Rim

672   (North American Cordellera, Paleozoic-Mesozoic orogenic belts in Asia and in

673   eastern New Zealand) in particular (Bierlein and Crowe 2000).

674

675   Mechanisms of mineralization

676

At Klipwal, gold mineralization is localized in a brittle-ductile, oblique-reverse, sinistral shear zone and associated fault splays. Gold is confined to laminated quartz veins within the sheared host rocks and also occurs in the alteration halo. It is postulated that the initial, auriferous, sulfur-rich, low salinity H_2O-CO_2-CH_4 fluid was transported to near-surface levels via a deep-rooted brittle-ductile shear zone, located at the contact of contrasting lithologic units and at a westward flexure of the KSZ, which acted as the favorable site for high-volume fluid flow. Pressure cycling (Robert et al. 1995) or the fault-valve mechanism (Sibson et al. 1988; Sibson 2001) is indicated by the presence of coexisting aqueous and carbonic inclusions that show wide variations in density (Fig. 12f). Although P-T values obtained by inclusion thermobarometry coupled with chlorite and arsenopyrite geothermometry (1.1 to 2.5 kbar and 265 to 315°C) are comparable with the P-T window of the orogenic gold deposits (Table 5), there is convincing evidence of near-isothermal pressure fluctuation (about 1.4 kbar). Pressure fluctuation facilitated phase separation of gaseous and aqueous fluid (Wilkinson and Johnston, 1996; Mikucki, 1998) resulting in a decrease in total sulfur content of the ore fluid, and leading to precipitation of free gold in quartz veins along with chlorite. Fluid-wall rock interaction, on the other hand, was responsible for the association of gold with sulfides where a decrease in fO$_2$ occurred (cf. Mikucki 1998). The presence of type-II pure CH_4 bearing inclusions and type-III CH_4-rich inclusions in close association with CO_2-rich carbonic inclusions is evidence for a decrease or fluctuation in ambient fO$_2$ conditions.

Timing of mineralization and source of ore fluid

The relative timing of mineralization is important for identifying the source of ore fluid and gold. Two possible models have been proposed for the source of gold-bearing hydrothermal fluid. These include (1) prograde metamorphic devolatilization of host rocks; (2) magmatic fluid originating from extensive regional or specific granitic intrusions (Hagemann and Cassidy 2000 and references therein; Tomkins 2013). Archaean orogenic lode gold mineralization, in general, is formed at a late stage in the tectono-magmatic evolution of the host terrane. Most of these gold-quartz lode veins are formed after peak metamorphism of the immediately surrounding host rocks, in greenschist facies deposits (Groves et al. 1998; Ridley and Diamond 2000; Goldfarb et al. 2001; Groves et al. 2003).

21

711   At Klipwal, the pyrite and arsenopyrite Re-Os data provide the timing of gold

712 mineralization at 2563±84 Ma. The initial Os isotope composition ($^{187}Os/^{188}Os_i$) from

713 these sulfide grains can be used to infer the source of sulfides and by inference ore

714 fluid and gold. In general, the mantle has relatively low amounts of Re, when

715 compared with crustal rocks, with respect to Os concentration (Kirk et al. 2002). This

716 is because crustal rocks are the products of partial melting of the mantle and

717 potentially re-melted products of previously formed crust. During partial melting Re

718 partitions more readily into the melt and as a result crustal rocks have higher Re/Os

719 values and thus rapidly evolve to develop elevated $^{187}Os/^{188}Os$ ratios (Kirk et al. 2002;

720 Kirk et al. 2003). The low non-radiogenic initial $^{187}Os/^{188}Os_i$ (0.29 ± 0.08) value

721 determined from the Re-Os data (Fig. 14) suggests that the sulfides and, by inference,

722 gold were originally derived from more primitive sources (cf. Reisberg et al 1991;

723 Selby 2007; Moreli et al. 2007), the most likely being mafic volcanic rocks in the

724 underlying Nsuze Group or mafic-ultramafic greenstone belts, such as the Nodweni

725 greenstone belt, which released non-radiogenic Os.

726   The post-Pongola granitic intrusions (between 2863 and 2721 Ma) had been

727 considered as a potential source of the ore fluid for the Klipwal mineralization.

728 However, fluid inclusion studies provided no evidence of magmatic fluid components

729 and Re-Os sulfide geochronology, even with the large error attached to the age date

730 (2563±84 Ma) shows that mineralization is much younger than the post-Pongola

731 granitic intrusions. Hence, there is no basis for relating these granites to gold

732 mineralization.

733   Instead, we propose that devolatilization during metamorphism of the Pongola

734 volcano-sedimentary sequence and perhaps deeper-seated greenstones of the

735 Kaapvaal basement, previously metamorphosed at sub-greenschist to greenschist

736 facies conditions, generated the required amounts of fluid. At sufficiently deep levels,

737 a second phase of metamorphism at higher temperatures would cause dehydration of

738 these rocks, with fluids migrating upwards and overprinting successively higher-level

739 rocks, whatever their original metamorphic grade. These fluids may have mixed with

740 mantle components or interacted with mafic to ultramafic rocks at depth, carrying

741 metals to shallow crustal levels with fluid flow locally focused into the Klipwal shear

742 zone, precipitating gold-quartz and carbonate veins.

743

744

22

757

758 **References**

759 Armstrong NV, Hunter DR, Wilson AH (1982) Stratigraphy and petrology of the

760   Archaean Nsuze Group, northern Natal and southeastern Transvaal, South Africa.

761   Precamb Res 19:75−107

762 Bailey SW (1988) Chlorites: structures and crystal chemistry. In Bailey SW (ed)

763   Hydrous Phyllosilicates. Rev Mineral 19:347−403

764 Bakker RJ (1997) CLATHRATES: Computer programs to calculate fluid inclusion V-

765   X properties using clathrate melting temperatures. Computers & Geosciences 23,

766   1-18

767 Bakker RJ (1999) Adaptation of the Bowers and Helgeson (1983) equation of state to

768   the H_2O-CO_2-CH_4-N_2-NaCl system. Chem Geol 154:225−236

769 Bakker RJ (2003) Package FLUIDS 1. Computer programs for analysis of fluid

770   inclusion data and modeling bulk fluid properties. Chem Geol 194: 3−23

771 Barnicoat AC, Henderson IHC, Knipe RJ, Yardley BWD, Napier RW, Fox NPC,

772   Kenyen AK, Muntingh DJ, Strydom D, Winkler KS, Lawrence SR, Cornford C

773   (1997) Hydrothermal gold mineralization in the Witwatersrand basin. Nature

774   386:820−824

775 Barton JM, Hunter DR, Jackson MPA, Wilson AC (1983) Geochronologic and Sr-

776   isotopic studies of certain units in the Barberton granite-greenstone terrain,

777   Swaziland. Transactions Geol Soc South Afr 86:71−80

778   Belonoshko AB, Saxena SK (1991) A molecular dynamics study of the pressure-
779   volume-temperature properties of super-critical fluids:II. CO_2,CH_4,CO,O_2 and H_2.
780   Geochm Cosmochim Acta 55:3191−3208

781   Bierlein FP, Crowe DE (2000) Phanerozoic orogenic lode gold deposits: Rev Econ
782   Geol 13:103−139

783   Bodnar RJ (1993) Revised equation and table for determining the freezing point
784   depression of H2O-NaCl solutions. Geochim. Cosmochim. Acta 57:683−684

785   Boulllier AM, Robert F (1992) Palaeoseismic events recorded in Abinbi gold-quartz
786   vein networks, Val d'or, Abitibi, Quebec,Canada. J Struct Geol 14:161−179

787   Bullen WD, Thomas RJ, McKenzie A (1994) Gold mineralization in Natal, South
788   Africa. J Afr Earth Sci 18: 99−109

789   Burke EAJ (2001) Raman microspectrometry of fluid inclusions. Lithos 55: 39−158

790   Cathelineau M, Nieva D (1985) A chlorite solid solution geothermometer The Los
791   Azufres (Mexico) geothermal system. Contrib Mineral Petrol 91:235−244

792   Chinnasamy SS, Mishra B (2013) Greenstone metamorphism, hydrothermal alteration
793   and gold mineralization in the genetic context of the granodiorite-hosted gold
794   deposit at Jonnagiri, eastern Dharwar craton, India. Econ Geol 108:1015−1036

795   Cooper RA, Tulloch AJ (1992) Early Palaeozoic terranes in New Zealand and their
796   relationship to the Lachlan fold belt. Tectonophysics 214:129−144

797   Cox SF, Knackstedt MA, Braun J (2001) Principles of structural control on
798   permeability and fluid flow in hydrothermal systems. In: Richards JP, Tosdal RM
799   (eds) Structural Controls on Ore Genesis. Rev Econ Geol 14:1 −24

800   Cumming VM, Poulton SW, Rooney AD, Selby D (2013) Anoxia in the terrestrial
801   environment during the late Mesoproterozoic. Geology 41:583−586

802   Cumming VM, Selby D, Lillis PG (2012) Re-Os geochronology of the lacustrine
803   Green River Formation: Insights into direct dating of lacustrine successions, Re-
804   Os systematics and paleocontinental weathering. Earth Planet Sci Lett 359:194−
805   205

806   de Ronde CEJ, Spooner ETC, de Wit MJ, Bray CJ (1992) Shear zone-related, Au
807   quartz vein deposits in the Barberton greenstone belt, South Africa: field and
808   petrographic characteristics, fluid properties, and light stable isotope
809   geochemistry. Econ Geol 87:366-402

810   Duan Z, Møller N, Weare JH (1992a) Molecular dynamics simulation of PVT
811   properties of geological fluids and a general equation of state of nonpolar and

weakly polar gases up to 2000 K and 20,000 bar. Geochim Cosmochim Acta 56:3839–3845

Duan Z, Møller N, Weare JH (1992b) An equation of state for the CH_4-CO_2-H_2O system: I. Pure systems from 0 to 1000°C and 0 to 8000 bar. Geochim Cosmochim Acta 56:2605–2617

Duan Z, Møller N, Weare JH (1992c). An equation of state for the CH_4-CO_2-H_2O system: II. Mixtures from 50 to 1000°C and 0 to 1000 bar. Geochim Cosmochim Acta 56:2619–2631

Dugdale AL, Hagemann SG (2001) The Bronzewing lode-gold deposit, Western Australia: P-T-X evidence for fluid immiscibility caused by cyclic decompression in gold-bearing quartz veins. Chem Geol 173:59–90

Elmer FL, White RW, Powell R (2006) Devolatilization of metabasic rocks during greenschist-amphibolite facies metamorphism J Metamor Geol 24:497–513

Fairmaid AM, Kendrick MA, Phillips D, Fu B (2011) The origin and evolution of mineralizing fluids in a sediment-hosted orogenic-gold deposit, Ballarat East, Southeastern Australia. Econ Geol 106: 653–666

Farrow DJ, Harmer RE, Hunter DR, Eglington BM (1990) Rb-Sr and Pb-Pb dating of the Anhalt leuco-tonalite, northern Natal. South Afr J Geol 93:696–701

Frimmel HE, Gartz VH (1997) Witwatersrand gold particle chemistry matches model of metamorphosed, hydrothermally altered placer deposits: Mineral Deposit 32:523–530

Frimmel HE, Hallbauer DK, Gartz VH (1999) Gold mobilizing fluids in the Witwatersrand Basin: composition and possible sources. Mineral Petrol 66:55– 81

Gao ZL, Kwak TAP (1995a) Turbidite-hosted gold deposits in the Bendgo-Ballart and Melbourne zones, Australia I: Geology, mineralization. Stable isotopes and implications for exploration. Int Geol Rev 37: 910–944

Gao ZL, Kwak TAP (1995b) Turbidite-hosted gold deposits in the Bendgo-Ballart and Melbourne zones, Australia II: Nature of ore fluids. Int Geol Rev 37:1007– 1038

Gold DJC (1993) The geological evolution of a part of the Pongola basin, southeastern Kaapvaal craton. Unpublished Ph.D. Thesis. University Natal, Pietermaritzburg, South Africa. pp 156

844   Gold DJC (2006) The Pongola Supergroup. In: Johnson MR, Anhaeusser CR, Thomas

845   RJ (eds) The Geology of South Africa. Geol Soc South Afr, Johannesburg,

846   Council for Geoscience 135–148

847   Gold DJC, Von Veh MW (1995) Tectonic evolution of the Late Archaean Pongola-

848   Mozaan basin, South Africa. J Afr Earth Sci 21:203–212

849   Goldfarb RJ, Baker T, Dube B, Groves DI, Hart CJR, Gosselin P (2005) Distribution,

850   character, and genesis of gold deposits in metamorphic terranes.In: Hedenquist

851   JW, Thompson JFH, Goldfarb RJ, Richards JP (eds) Economic Geology. 100th

852   Anniversary Volume 1905–2005. Littleton, Colorado, Society of Economic

853   Geologists 407–450

854   Goldfarb RJ, Christie T, Skinner D, Haeussler P, Bradley D (1995) Gold deposits of

855   Westland, New Zealand and southern Alaska. Products of the same tectonic

856   processes? In: Mauk J (ed) PACRIM '95. Symp 239–244

857   Goldfarb RJ, Groves DI, Gardoll S (2001) Rotund versus skinny orogens: well-

858   nourished or malnourished gold? Geology 29:539–542

859   Goldfarb RJ, Phillips GN, Nokleberg WJ (1998) Tectonic setting of synorogenic gold

860   deposits of the Pacific Rim. Ore Geol Rev 13:85–218

861   Goldfarb RJ, Snee LW, Miller LD, Newberry RJ (1991) Rapid dewatering of the crust

862   deduced from ages of mesothermal gold deposits. Nature 354:296–298

863   Goldfarb RJ, Snee LW, Pickthorn WJ (1993) Orogenesis, high-T thermal events, and

864   gold vein formation within metamorphic rocks of the Alaskan Cordillera. Mineral

865   Mag 57: 375–394

866   Groves DI, Goldfarb RJ, Robert F, Hart CJR (2003) Gold Deposits in Metamorphic

867   Belts: Overview of Current Understanding, Outstanding Problems, Future

868   Research, and Exploration Significance. Econ Geol 99:1–29

869   Groves DI. Goldfarb RJ, Gebre-Mariam M, Hagemann SG, Robert F (1998) Orogenic

870   gold deposits: a proposed classification in the context of their crustal distribution

871   and relationship to other gold deposit types. Ore Geol Rev 13:7–27

872   Hagemann SG, Bray C, Brown PE, Spooner ETC (1996) Combined gas and ion

873   chromatography of fluid inclusions and sulfides from the Archean epizonal

874   Wilualode gold deposits, Western Australia. In: Brown PE, Hegemann SG (eds)

875   Pan-American conference on research on fluid inclusions 6: Program and abstract:

876   Wisconsin, Department of Geology and Geophysics, University of Wisconsin-

877   Madison, 56–58

878 Hagemann SG, Brown PE (1996) Geobarometry in Archean lode gold deposits: Eur J
879   Mineral 8:937–960

880 Hagemann SG, Brown PE (2000) Gold in 2000: An Introduction. Rev Econ Geol 13:
881   1–7

882 Hagemann SG, Cassidy KF (2000) Archaean orogenic lode gold deposits: Rev Econ
883   Geol 13:9–68

884 Hagemann SG, Gebre-Mariam M, Groves DI (1994) Surface-water influx in shallow-
885   level Archean lode gold deposits in Western Australia, Geology 22:1067–1070

886 Hallbaner DK, Utter T (1977) Geochemical and morphological characteristics of gold
887   particles from recent river deposits and the fossil placers of the Witwatersrand.
888   Miner Depos 12: 293–306

889 Hartwig E, Frimmel HE (2002) Genesis of the World's Largest Gold Deposits.
890   Science 297:1815–1817

891 Hegner E, Kröner A, Hofmann AW (1984) Age and isotopic geochemistry of
892   Archaean Pongola and Usushwana suites in Swaziland, southern Africa: a case for
893   crustal contamination of mantle-derived magma. Earth Planet Sci Lett 70:267–279

894 Hegner E, Kröner A, Hofmann AW (1993) Trace element and isotopic constrains on
895   the origin of the Archaean Pongola and Usushwana Igneous Suites in Swaziland.
896   In: Maphalala R, Mabuza m (Compliers), Extended Abstract: 16th International
897   Colloquium on African Geology, Geological Survey and Mines Department,
898   Swaziland pp 147–149

899 Hilliard P (2007) A structural evaluation of the Kilpwal Gold Mine, Unpublished
900   Mine Report, Bosveld Mines (Pty) Ltd pp 15

901 Ho SE (1987) Fluid inclusions: Their potential as an exploration toll for Archean gold
902   deposits. In: Ho SE, Groves DI (eds) Recent advances in understanding
903   Precambrian gold deposits: Geology Department and University Extension,
904   University of Western Australia, Publication No 11:239–263

905 Ho SE, Bennett JM, Cassydy KF, Hronsky JMA, Mikucki EJ, Sang JH (1990) Nature
906   of ore fluid, and transportational and depositional conditions in sub-amphibolite
907   facies deposits In: Ho SE, Groves DI, Bennett JM (eds) Gold deposits of the
908   Archean Yilgarn Block, Western Australia: Nature, genesis and exploration
909   guides: Geology Department (Key Centre) and University Extension, University
910   of Western Australia, Publication no 20:198-211

911   Holland TJB, Baker J, Powell R (1998) Mixing properties and activity-composition
912   relationship of chlorite in the system MgO-FeO-Al$_2$O$_3$-SiO$_2$-H$_2$O. Eur J Mineral
913   10:395−406

914   Horvath P, Reinhardt J, Hofmann A (2014) High-grade metamorphism of ironstones
915   in the Mesoarchaean of southwest Swaziland. Mineral Petrol 108:589-605

916   Hunter DR, Smith RG, Sleigh DWW (1992) Geochemical studies of Archaean
917   granitoid rocks in the Southeastern Kaapvaal Province: Implications for crustal
918   development J Afr Earth Sci 15:127−151

919   Jacobs GK, Kerrick DM (1980) Methane: An equation of state with application to the
920   ternary system H$_2$O-CO$_2$-CH$_4$, Geochim Cosmochim Acta 45:607−614

921   Kamo SL, Davis DW (1994) Reassessment of Archean crustal development in the
922   Barberton Mountain Land, South Africa, based on U-Pb dating Tectonics 13:167−
923   192

924   Kerrich R, Cassidy KF (1994) Temporal relationships of lode gold mineralization to
925   accretion, magmatism, metamorphism and deformation, Archaean to present: A
926   review. Ore Geol Rev 9:263−310

927   Kirk J, Ruiz J, Chesley J, Titley S (2003) The Origin of Gold in South Africa.
928   American Scientist 91:534−541

929   Kirk J, Ruiz J, Chesley J, Titley S, Walshe J (2001) A detrital model for the origin of
930   gold and sulfides in the Witwatersrand basin based on Re−Os isotopes. Geochim
931   Cosmochim Acta 65:2149−2159

932   Kirk J, Ruiz J, Chesley J, Walshe J, England G (2002) A major Archean gold and
933   crust-forming event in the Kaapvaal Craton, South Africa. Science 297:1856−
934   1858

935   Kisters AFM, Kolb J, Meyer FM, Hoernes S, (2000) Hydrologic segmentation of
936   high-temperature shear zones: structural, geochemical and isotopic constraints
937   from auriferous mylonitesof the Renco Mine, southern Zimbabwe. J Struct Geol
938   22:811 −829

939   Knipe RJ, McCaig AM (1994) Microstructural and microchemical consequences of
940   fluid flow in deforming rocks. In: Parnell J (ed) Geofluids: Origin, Migration and
941   Evolution of Fluid in Sedimentary Basins. Geol Soc Special Publication pp 99−
942   112

943   Kolb J,   Rogers A, Meyer F M, Vennemann TW   (2004) Development of fluid
944   conduits in the auriferous shear zones of the Hutti Gold Mine, India: evidence for
945   spatially and temporally heterogeneous fluid flow. Tectonophysics 378:65– 84

946   Kretschmar U, Scott SD (1976) Phase relations involving arsenopyrite in the system
947   Fe-As-S and their application. Can Mineral 14:364–386

948   Kretz R (1983) Symbols for rock-forming minerals. Am Mineral 68:277–279

949   Krienitz M-S, Trumbull RB, Hellmann A, Kolb J, Meyer FM, Wiedenbeck M (2008)
950   Hydrothermal gold mineralization at the Hira Buddini gold mine, India: Constraints
951   on fluid evolution and fluid sources from boron isotopic compositions of tourmaline.
952   Miner Depos 43:421–434

953   Lawley C, Selby D, Imber J (2013) Re-Os Molybdenite, Pyrite, and Chalcopyrite
954   Geochronology, Lupa Goldfield, Southwestern Tanzania: Tracing Metallogenic
955   Time Scales at Midcrustal Shear Zones Hosting Orogenic Au Deposits. Econ Geol
956   108:1591–1613

957   Layer PW. Kröner A, McWilliams M, Burghele A (1988) Paleomagnetism and age of
958   the Archean Usushwana Complex, southern Africa. J of Geophy Res 93:449–457

959   Ludwig K R (1980) Calculation of uncertainties of U-Pb isotope data. Earth Plan Sci
960   Let, 46:212–220

961   Mancktelow NS, Grujic D, Johnson EL (1998) An SEM study of porosity and grain
962   boundary microstructure in quartz mylonites, Simplon Fault Zone, Central Alps.
963   Contrib Mineral Petrol 131:71–85

964   Maphalala R, Kröner A (1993) Pb-Pb single zircon ages for the younger Archaean
965   granitoids of Swaziland, southern Africa. In: Maphalala R Mabuz M (eds)
966   Extended Abstracts 16th Colloquium of African Geology.

967   Matthews PE (1990) A plate tectonic model for the Late Archaean Pongola
968   Supergroup in southeastern Africa. In: Sychanthavong SPH (ed), Crustal
969   Evolution and Orogeny. Oxford and IBH Publishing New Delhi pp 41–73

970   Matthews PE, Chatlesworth G, Eglington BM, Harmer RE (1989) A minimum 3.29
971   Ga age for the Nondweni greenstone complex in the south-eastern Kaapvaal
972   Craton. South Afr J Geol 92:272–278

973   McCaig AM (1997) The geochemistry of volatile fluid flow in shear zones. In:
974   Holness, MB (ed) Deformation Enhanced Fluid Transport in the Earth's Crust and
975   Mantle. Mineral Soc Series London pp 227–266

976   McCuaig TC, Kerrich R (1998) P-T-t-deformation-fluid characteristics of lode gold
977   deposits: evidence from alteration systematics. Ore Geol Rev 12:381–453

978   Mernagh TP (1996) Gold mineralization at Mount Charlotte: Evidence for fluid
979   oxidation from fluid inclusions: Geol Soc Australia, Abstracts 41 p 292

980   Mikucki EJ (1998) Hydrothermal transport and depositional processes in Archean
981   lode-gold systems: A review. Ore Geol Rev 13:307–321

982   Mikucki EJ (1998) Hydrothermal transport and depositional processes in Archean
983   lode-gold systems: A review. Ore Geol Rev 13:307-321

984   Mikucki EJ, Ridley JR (1993) The hydrothermal fluid of Archaean lode-gold deposits
985   at different metamorphic grades: compositional constraints from ore and wall rock
986   alteration assemblages. Miner Depos 28:469–481

987   Miller LD, Goldfarb RJ, Snee LW, Gent CA, Krikham RA (1995) Structural geology,
988   age, and mechanisms of gold vein formation at the Kensington and Julian
989   deposits, Berners Bay district, southeast Alaska. Econ Geol 90:343–368

990   Minter WEL (1999) Irrefutable detrital origin of Witwatersrand gold and evidence of
991   aeolian signatures: Econ Geol 94:665–670

992   Mishra B, Pal N (2008) Metamorphism, Fluid Flux, and Fluid Evolution Relative to
993   Gold Mineralization in the Hutti-Maski Greenstone Belt, Eastern Dharwar Craton,
994   India Econ Geol 103:801–827

995   Mishra B, Panigrahi MK (1999) Fluid evolution in the Kolar gold field: evidence
996   from fluid inclusion studies. Miner Depos 34:173-181

997   Morelli R, Creaser RA, Seltmann R, Stuart FM, Selby D, Graupner T (2007) Age and
998   source constraints for the giant Muruntau gold deposit, Uzbekistan, from coupled
999   Re-Os-He isotopes in arsenopyrite. Geology 35:795–798

1000 Mueller AG, Groves DI (1991) The classification of Western Australian greenstone-
1001   hosted gold deposits according to wall rock alteration mineral assemblages. Ore
1002   Geol Rev 6:291-331

1003 Mukasa SB, Wilson AH, Young KR (2013) Geochronological constraints on the
1004   magmatic and tectonic development of the Pongola Supergroup (Central Region),
1005   South Africa. Precamb Res 224:268–286

1006 Nokleberg WJ, Bundtzen TK, Dawson KM et al (1996) Significant metalliferous lode
1007   deposits and placer districts for the Russian Far East, Alaska and the Canadian
1008   Cordillera: United States Geological Survey Open-File report 96-513-A p 385

Nokleberg WJ, Plafker G, Wilson FH (1994) Geology of south-central Alaska. In: Plafker G Berg HC (eds) The Geology of Alaska. Geol. Soc. Am G-1 pp. 311–366

Pal N, Mishra B (2002) Alteration geochemistry and fluid inclusion characteristics of the greenstone hosted gold deposit at Hutti, Eastern Dharwar Craton, India. Miner Depos 37:722–736

Peters SG, Golding SD, Dowling K (1990) Melange- and sediment-hosted gold-bearing quartz veins, Hodgkinson gold field, Queensland, Australia. Econ Geol 85:312–327

Phillips GN, Hughes MJ (1996) The geology and gold deposits of the Victorian gold province. Ore Geol Rev 11:255–302

Phillips GN, Law JDM (2000) Witwatersrand gold fields: geology, genesis and exploration. Rev Econ Geol 13:439–500

Pouchou JL Pichoir F (1984) A new model for quantitative X-ray microanalyses, Part I: application to the analyses of homogenous samples. Recherche Aerospatiale, 3:13–36

Pretorius DA (1981) Gold and uranium in quartz-pebble conglomerates. Econ Geol 75th Anniversary Volume pp 117–138

Ramsay WRH, Bierlein FP, Arne DC, Vandenberg AHM (1998) A review of turbidite-hosted gold deposites central Victoria: regional setting, styles of mineralluzation and genetic constrains Ore Geol Rev 13:131–151

Reimold WU, Meyer FM, Walraven F, Matthews PE (1993) Geochemistry and chronology of Pre- and post-Pongola granitoids from northeastern Natal. In: Maphalala R, Mabuza M (eds) Extended Abstracts from the 16th Colloquium on African Geology, Geol Survey Mbabane Swaziland. 294–296

Reisberg LC, Allrgre CJ, Luck J-M (1991) The Re-Os systematics of the Ronda Ultramafic Complex of southern Spain Earth Planet Sci Lett 105: 196–213

Ridley JR, Diamond LW (2000) Fluid chemistry of orogenic lode gold deposits and implications for genetic models. Rev Econ Geol 13:141–162

Robb LJ, Brandl G, Anhaeusser CR, Poujol M (2006) Archaean granitoid intrusions of the Kaapvaal Craton. In: Johnson MR, Anhaeusser CR, Thomas RJ (eds) The Geology of South Africa. Geol Soc South Afr Council for Geoscience pp 57–94

Robb LJ, Meyer FM (1995) The Witwatersrand Basin, South Africa: Geological framework and mineralization processes. Ore Geol Rev 10:67–94

1042 Robert F, Boullier AM, Firdaous K (1995). Gold–quartz veins in metamorphic
1043   terranes and their bearing on the role of fluids in faulting. J Geophy Res
1044   100:12861–12879

1045 Robert F, Brown AC (1986) Archaean gold-bearing quartz veins at the Sigma mine,
1046   Abitibi greenstone belt, Quebec. Part I. Geologic relations and formations of the
1047   vein systems. Econ Geol 81:578–592

1048 Robert F, Kelly WC (1987) Ore forming fluids in Archaean gold-bearing quartz veins
1049   at the Sigma Mine, Abitibi greenstone belt, Quebec, Canada. Econ Geol 82:1464-
1050   1482

1051 Robert F, Poulsen KH (2001) Vein fomation and deformation in greenstone gold
1052   deposits. In: Richards JP, Tosdal RM (eds) Structural control on ore genesis. Rev
1053   Econ Geol 14:111-155

1054 Roedder E, Bodnar RJ (1980) Geologic pressure determination from fluid inclusion
1055   studies. Ann Rev Earth Plan Sci 8:263–301

1056 Roering C (1968) The tectonics of the West Rand Syncline: A field study of brittle
1057   failure in the Witwatersrand Basin, Econ Geol Unit Univ. Witwatersrand
1058   Johannesburg Inform Circ 48: pp 28

1059 Saggerson EP, Turner, LM (1995) A Review of Metamorphism in the Republic of
1060   South Africa and the Kingdoms of Lesotho and Swaziland. Explanation of
1061   Metamorphic Map 1: 1 000 000. Council for Geoscience, Pretoria, 285 pp.

1062 Saravanan CS, Mishra B, Jairam MS (2009) P-T conditions of mineralization in the
1063   Jonnagiri granitoid-hosted gold deposit, eastern Dharwar craton, southern India:
1064   Constraints from fluid inclusions and chlorite thermometry. Ore Geol Rev
1065   36:333–349

1066 Scholz CH (1988) The brittle-plastic transition and the depth of seismic faulting.
1067   Geologische Rundschau 77:319–328

1068 Selby D (2007) Direct rhenium-osmium age of the Oxfordian-Kimmeridgian
1069   boundary, Staffin bay, Isle of Skye, UK and the Late Jurassic time scale.
1070   Norwegian Jour Geol 87:291–299

1071 Selby D, Kelley KD, Hitzman MW, Zieg J (2009) Re-Os sulfide (bornite,
1072   chalcopyrite, and pyrite) systematics of the carbonate-hosted copper deposits at
1073   Ruby Creek, southern Brooks Range, Alaska. Econ Geol 104:437–444

1074 Sharp ZD, Essene, EJ, Kelly, WC (1985) A reexamination of the arsenopyrite
1075   geothermometer: pressure considerations and applications to natural assemblages.
1076   Can Mineral 23:517–534

1077 Sibson RH, Robert F, Poulsen H (1988) High angle faults, fluid pressure cycling and
1078   mesothermal gold-quartz deposits. Geology 16:551–555

1079 Sibson, RH (2001) Seismogenic framework for hydrothermal transport and ore
1080   deposition. In: Richards JP, Tosdal RM (eds) Structural Control on Ore Genesis.
1081   Rev Econ Geol 14:25–50

1082 Sinha M (1997) Gold mineralization in the western Ramagiri block, Anantapur
1083   district, Andhra Pradesh, with special reference to fluid inclusion characteristics.
1084   Unpublished MSc. Thesis Indian Institute of Technology Kharagpur.

1085 Smith TJ, Cloke PL, Kesler SE, (1984) Geochemistry and fluid inclusions from the
1086   McIntyre-Hollinger gold deposit, Timmins, Ontario, Canada Econ Geol
1087   79:1265–1285

1088 Smoliar MI, Walker RJ, Morgan JW (1996) Re-Os constraints on the age of Group
1089   IIA, IIIA, IVA, and IVB iron meteorites: Science 271:1099–1102

1090 Spooner ETC, Bray CJ, Wood PC, Burrows DR, Callan NJ (1987) Grant 236. Au-
1091   quartz vein and Cu-Au-Ag-Mo-Anydrite mineralization, Hollinger-McIntyre
1092   mines, Timmins, Ontario: $\delta^{13}C$ values (McIntyre), fluid inclusion gas chemistry,
1093   pressure (depth) estimation and H_2O-CO_2 phase separation as a precipitation and
1094   dilation mechanism. Ontario Geological Survey, Miscellaneous Paper 136:33–36

1095 Stipp M, Stunitz H, Heilbronner R, Schmid SM (2002) The eastern Tonale fault zone:
1096   A "natural laboratory" for crystal plastic deformation of quartz over a temperature
1097   range from 250 to 700ºC. J Struct Geol 24:1861–1884

1098 Thiéry R, Videl J, Dubessy J (1994) Phase equilibria modeling applied to fluid
1099   inclusions. Liquid–vapor equilibria and calculation of the molar volume in the
1100 CO_2-CH_4-N_2 system. Geochim Cosmochim Acta 58:1073–1082

1101 Thomas RJ, Verbeek JA, Walraven F (1995) Geology of the Archaean Nzimane
1102   Inlier, Zululand. Abstract, Centen. Geocongress Geol Soc South Afr pp 200–203

1103 Tomkin AG (2013) On the source of orogenic gold. Geology 41:1255–1256

1104 Touret JLR (2001) Fluid inclusions in metamorphic rocks. Lithos 55:1–25

1105 Vidal O, De Andrade V, Lewin E, Munoz M, Parra T, Pascarelli S (2006) P-T-
1106   deformation-Fe^{3+}/Fe^{2+} mapping at the thin section scale and comparison with

1107   XANES mapping. Application to a garnet-bearing metapelite from the
1108   Sambagawa metamorphic belt (Japan). J Metamorphic Geol 24:669–683

1109 Vidal O, Parra T, Trotet F (2001) A thermodynamic model for Fe-Mg aluminous
1110   chlorite using data from phase equilibrium experiments and natural pelitic
1111   assemblages in the 100-600°C, 1-25 kbar P-T range. Am J Sci 301:557–592

1112 Vidal O, Parra T, Vieillard P (2005) Thermodynamic properties of the Tschermak
1113   solid solution in Fe-chlorites: Application to natural examples and possible role of
1114   oxidation. Am Mineral 90:359–370

1115 Wilkinson JJ, Johnston JD (1996) Pressure fluctuations, phase separation, and gold
1116   precipitation during seismic fracture propagation. Geology 24:395–398

1117 Wilson AC, Jackson MPA (1988) Mantled gneiss domes in southern Swaziland and
1118   the concept of 'stable' Pongola cratonic cover. S. Afr. J. Geol 91:404–414

1119 Zang W Fyfe WS (1995) Chloritization of the hydrothermally altered bedrock at the
1120   Igarape Bahia gold deposit, Carajás, Brazil. Miner Depos 30:30–38

1121 Zhang Y, Frantz JD (1987) Determination of homogenization temperature and
1122   densities of supercritical fluid in the system $NaCl-KCl-CaCl_2-H_2O$ using synthetic
1123   fluid inclusions. Chem Geol 64:335–350

1124

1125 **List of Figures**
1126
1127 Fig. 1. (a) Locality map showing position of the main Pongola basin in South Africa.
1128 (b) Regional geological map of the Pongola basin showing major structural features
1129 (modified after Gold 2006). (c) Geological map of the Klipwal Gold Mine showing
1130 the Klipwal Shear Zone within rocks of the Mozaan Group (modified after Gold and
1131 Von Veh 1995). PR: Piet Retief; P: Pongola.

1132

1133 Fig. 2. (a) Subsurface geological cross section across the Klipwal Shear Zone showing
1134 disposition of various reefs and alteration halos (modified after Hilliard 2007). (b)
1135 Poles to the shear zone foliation; equal area lower hemisphere projection. See text for
1136 discussion.

1137

1138 Fig. 3. Field photographs from Klipwal mine area (a) showing old mine excavation
1139 with siltstone in footwall and sandstone in the hanging wall. (b) Slickensides (dashed
1140 lines) on the siltstone surfaces. (c) Shear related fold with NW trending axial planar
1141 fabric (broken line). (d) Sheared and mylonitized fabric in sandstone.

1142

1143 Fig. 4. Underground mine photographs showing different features of shear zone,
1144 laminated fault-fill quartz veins and alteration zones. (a) Laminated quartz vein in the
1145 inner zone preserving S-C fabric with sinistral sense of shear. (b) Oblique S-C fabric
1146 with sinistral sense of shear in the wall rock mylonites along with quartz shear lenses.

1147   (c) Sub-horizontal extension vein arrays associated with fault-fill vein in the shear
1148   zone. (d) Fault gouge in the R-reef showing fault breccia with fragments of host rocks
1149   and quartz veins and mylonites. (e) Extensional veins are displaced by the later faults.
1150   (f) H-reef fault-fill quartz vein and mylonitic shear zone contact with absence of fault
1151   breccia.
1152

1153   Fig. 5. Geological map along a crosscut from the main drive (R-reef) at level 10
1154   which cuts across H- and J- reefs. Stars denote the sample locations. The map shows
1155   underground geology, alteration halos around the reefs and the attitude of shear
1156   foliation in the quartz veins.
1157

1158   Fig. 6. Photomicrographs showing mineralogical and structural features of least
1159   altered and altered host rocks in the proximal zone. Photographs a to d, f: + Pol; e:
1160   plane-polarized light. See text for discussion. Mineral abbreviations are after Kretz
1161   (1983). Car: carbonates.
1162

1163   Fig. 7. Photomicrographs showing the mineralogical and structural features of the
1164   auriferous laminated quartz veins in the inner zone. (a) Alternating laminae consisting
1165   of quartz + dolomite and muscovite + chlorite. (b) S-C fabric within the lamina
1166   showing sinistral sense of shear. (c) Plastic deformation structures in quartz grains. (d)
1167   Quartz shear lens within the mylonites. (e) Fragments of quartz vein with brittle
1168   fractures and mylonite clasts in fault breccia. (f) Brittle fractures in the arsenopyrite
1169   and pyrite grains are filled with quartz and chlorite; quartz strain fringes with chlorite.
1170   (g) Silicate inclusion trails within sulfides showing relationship between sulfide
1171   growth and shear foliation. (h) Sketch of (g) for clear illustration. All photographs are
1172   taken under + Pol, except (e and g). See text for discussion. Mineral abbreviations are
1173   after Kretz (1983).
1174

1175   Fig. 8. Reflected light photomicrographs and BSE images showing different types of
1176   pyrites. (a) Three textural types of pyrite. (b) Coexisting pyrite-I and arsenopyrite-I
1177   along with pyrite-II inclusions within arsenopyrite-I. (c) Gold (Au) and chalcopyrite
1178   inclusions within pyrite-I with arsenopyrite-II at pyrite-I boundary. (d) Chalcopyrite,
1179   pyrrhotite and arsenopyrite-II inclusions within pyrite-II. (e) Euhedral pyrite-I grains
1180   with silicate inclusions and As-poor zone (dotted line). (f) Pyrite-II overgrows on
1181   pyrite-I (dotted line). (g) Concentric As-poor and As-rich zones in pyrite-II. (h)
1182   Irregular As zoning in pyrite-II. All photographs were taken in plane-polarized light.
1183   Mineral abbreviations are after Kretz (1983).
1184

1185   Fig. 9. Summary of different textural types of pyrite and arsenopyrite, in the inner and
1186   proximal alteration zone, with schematic sketches. Mineral abbreviations are after
1187   Kretz (1983)
1188

1189   Fig. 10. Reflected light photomicrographs in plane-polarized light showing occurrence
1190   of gold in the Klipwal deposit. (a) Gold (Au) inclusions within pyrite-I at the contact
1191   of chalcopyrite grain. (b) Gold as isolated inclusion within pyrite-I. (c) Inclusion of
1192   gold grain within arsenopyrite-II. (d) Free gold grain in quartz matrix, sharing the
1193   grain boundary with chlorite (Chl). Mineral abbreviations are after Kretz (1983).
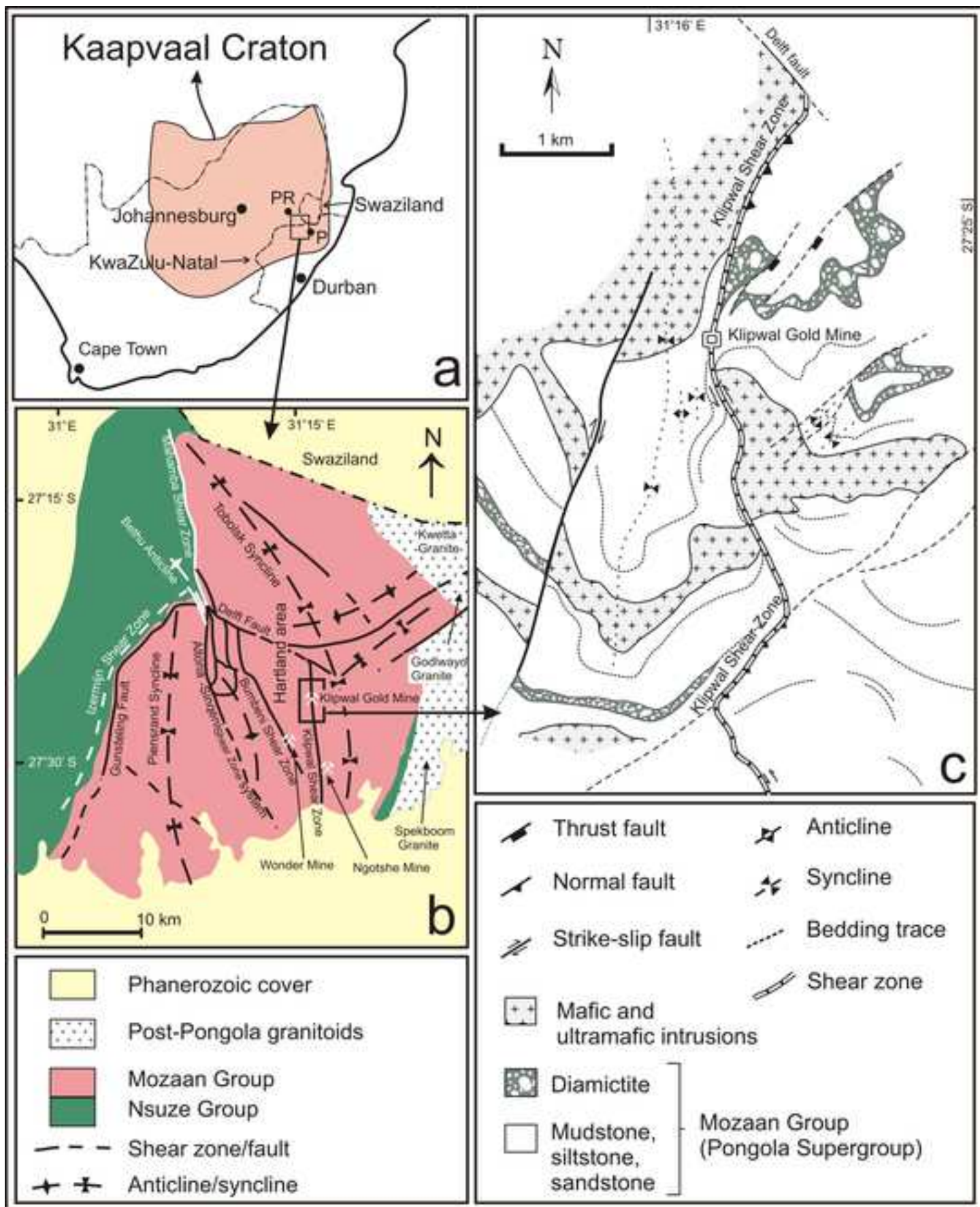1194

1195   Fig. 11. Representative photomicrographs and Raman spectra of different fluid
1196   inclusion types. (a) Isolated type-I inclusion. (b) Occurrence of type-II and type-III
1197   inclusions in the same 3-dimenstioanl cluster. (c) Representative Raman spectrum of
1198   type-II inclusions showing CH_4 peak at 2912 cm^{-1}. (d) Raman spectrum of type-III
1199   inclusions showing CO_2 doublets (at 1283 and 1388 cm^{-1}) and presence of CH_4 (at
1200   2913 cm^{-1}). (e) Intra-granular trail of type-IV inclusions. (f) Coexisting type-III (C)
1201   and type-IV (A) inclusions in one group of synchronous inclusions (GSI).
1202

1203   Fig. 12. Histogram plots of fluid inclusion microthermometric data. (a) Temperatures
1204   of CH_4 vapor homogenization of type-II inclusions, (b) Temperatures CO_2 ice melting
1205   and (c) Homogenization of type-III inclusions, (d) Last ice melting and (e) Liquid
1206   vapor homogenization temperatures of type-IV inclusions, (f) $T_{h,CO2}$ versus $T_{m,CO2}$
1207   plot for pure CO_2 type-III inclusions showing density variation.
1208

1209   Fig. 13. Isochore plot constructed using the minimum and maximum densities of each
1210   type of inclusions. Figures indicate the density values (in g/cm^3) for respective
1211   inclusions. P-T estimation by (i) intersecting isochores of type-III (solid lines) and
1212   type-IV (dashed lines) inclusions (ii) intersection of chlorite thermometer (CT) and
1213   (iii) arsenopyrite thermometer (AT) with the isochores. The box illustrates the P-T
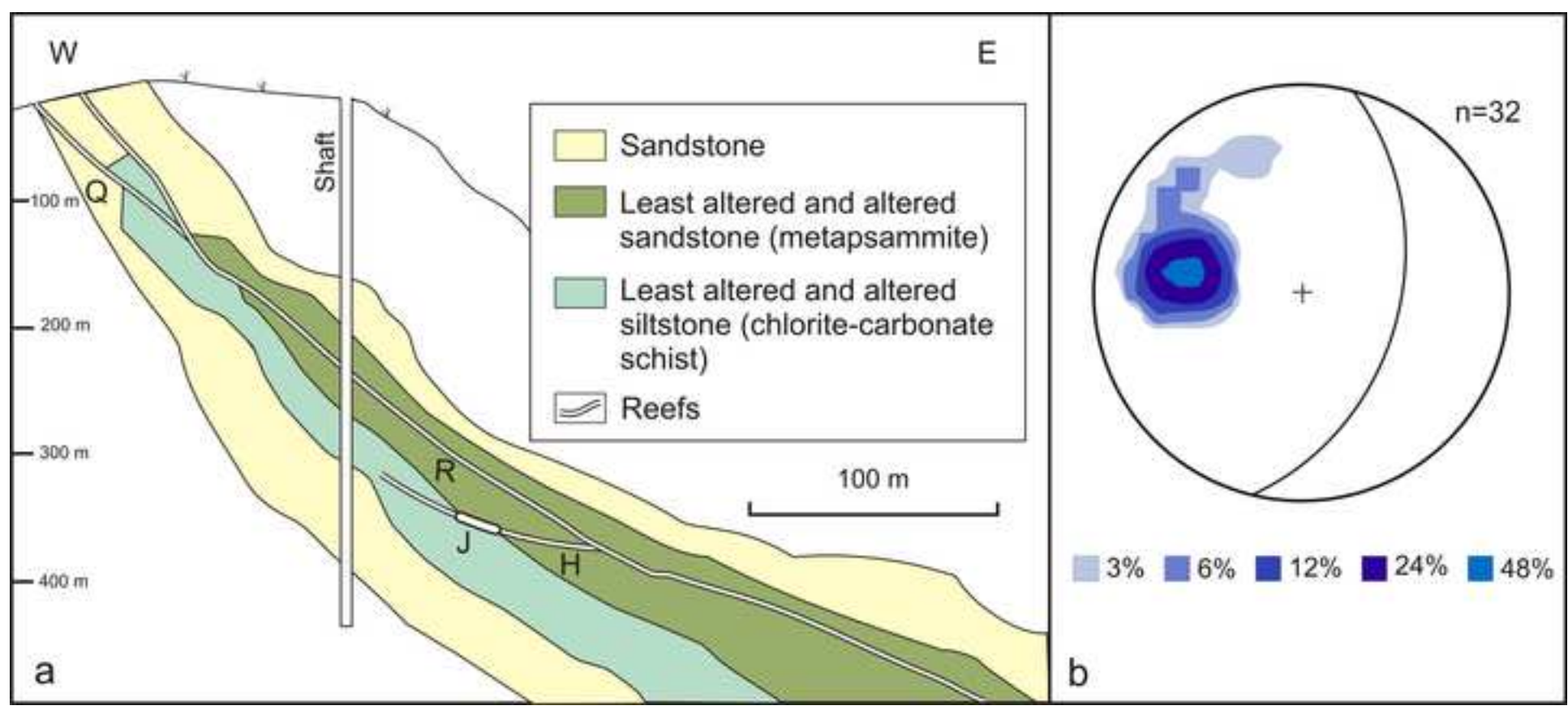1214   domain of gold mineralization at Klipwal. IS-1 and IS-2 denotes isochore intersection.
1215

1216   Fig. 14. $^{187}Re/^{188}Os$ vs. $^{187}Os/^{188}Os$ isochron plot for pyrite and arsenopyrite grains
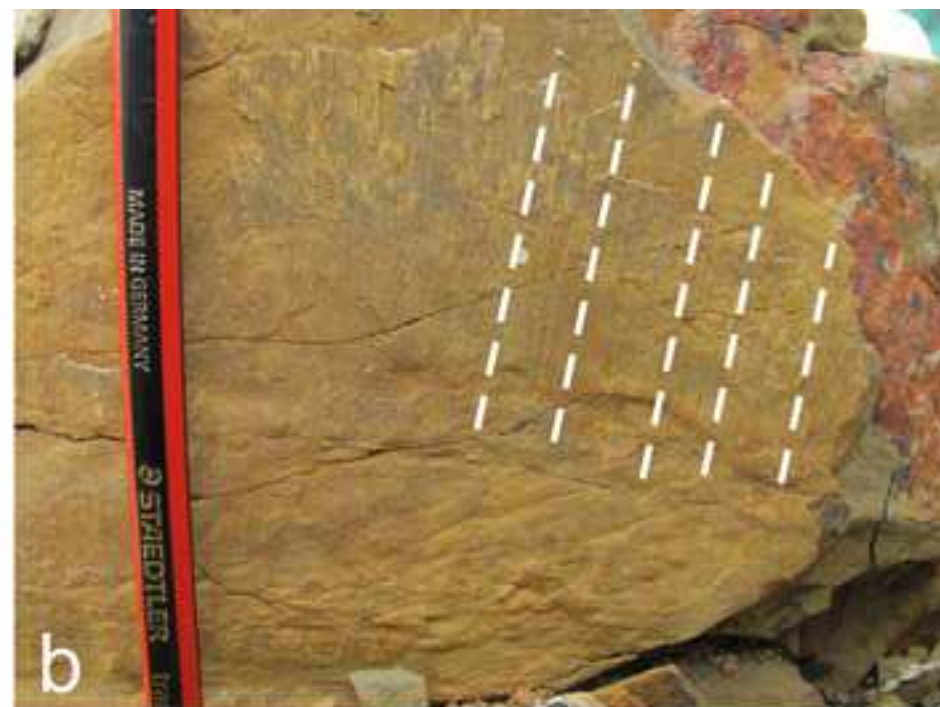1217   from the ore zone. See text for discussion.

Figure
Click here to download high resolution image

Kaapvaal Craton

Johannesburg

Swaziland

KwaZulu-Natal

Durban

Cape Town

a

31°E   31°15' E

Swaziland

N

27°15' S

Kwetta Granite

Godwayo Granite

Klipwal Gold Mine

Spekboom Granite

Wonder Mine   Ngotshe Mine

27°30' S

0   10 km

b

31°16' E

N

1 km

Delft fault

Klipwal Shear Zone

Klipwal Gold Mine

Klipwal Shear Zone

c

Thrust fault   Anticline

Normal fault   Syncline

Strike-slip fault   Bedding trace

Shear zone

Mafic and
ultramafic intrusions

Diamictite

Mudstone,
siltstone,
sandstone

Mozaan Group
(Pongola Supergroup)

Phanerozoic cover

Post-Pongola granitoids

Mozaan Group

Nsuze Group

Shear zone/fault

Anticline/syncline

W   E

Shaft

- 100 m Q
- 200 m
- 300 m R
          J
          H
- 400 m

Sandstone

Least altered and altered sandstone (metapsammite)

Least altered and altered siltstone (chlorite-carbonate schist)

Reefs

100 m

a

n=32

+

3% 6% 12% 24% 48%

b

J-reef

H-reef

R-reef

F *

G *

E *

50

C * D *

52

55

B *

A *

N

10 m

Level: 10
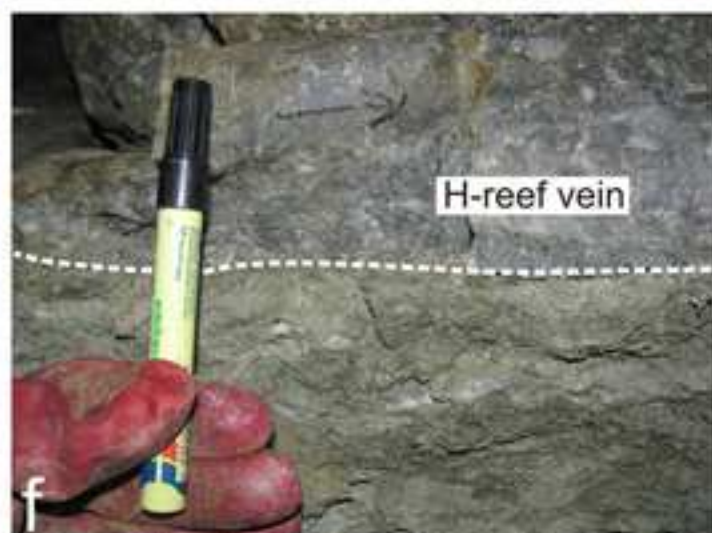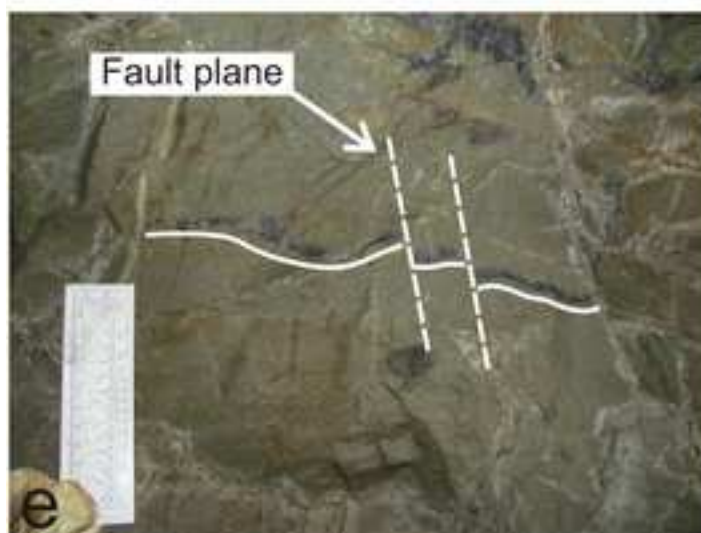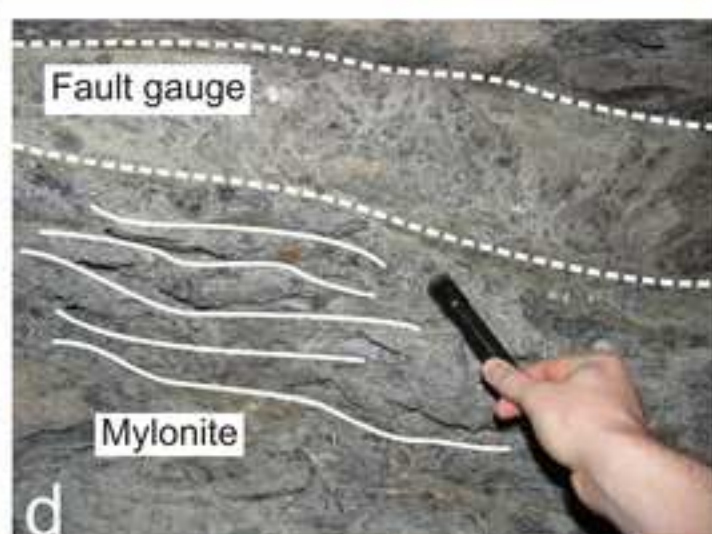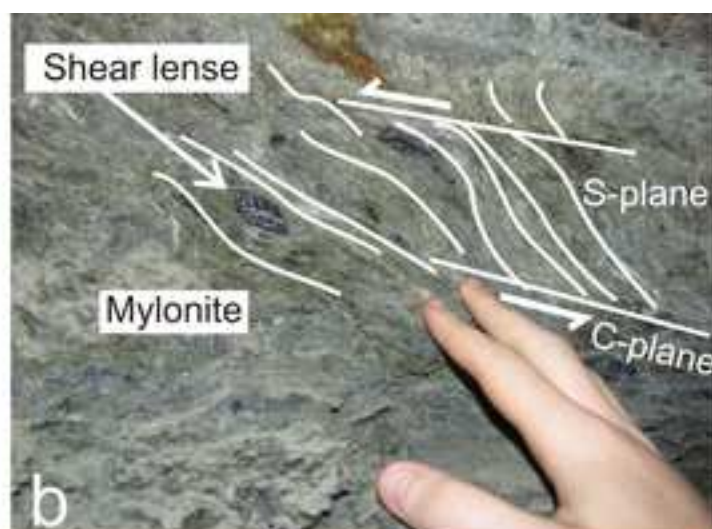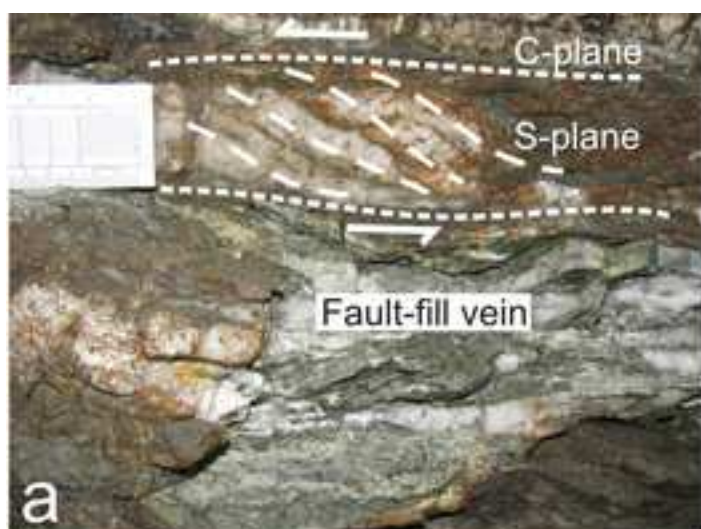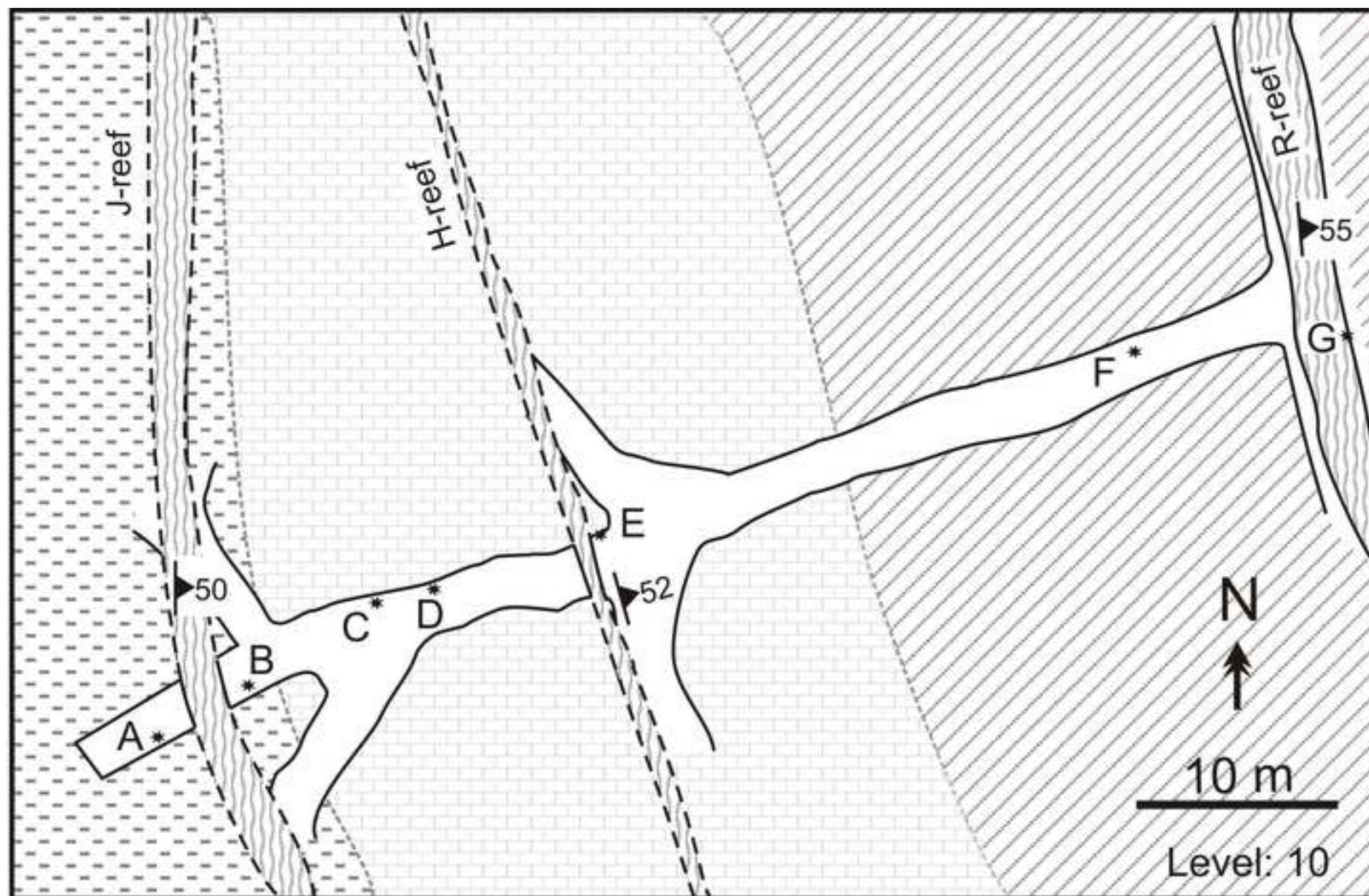
Altered siltstone
(Chlorite-Carbonate schist)

Least-altered sandstone

Altered sandstone
(Metapsammite)
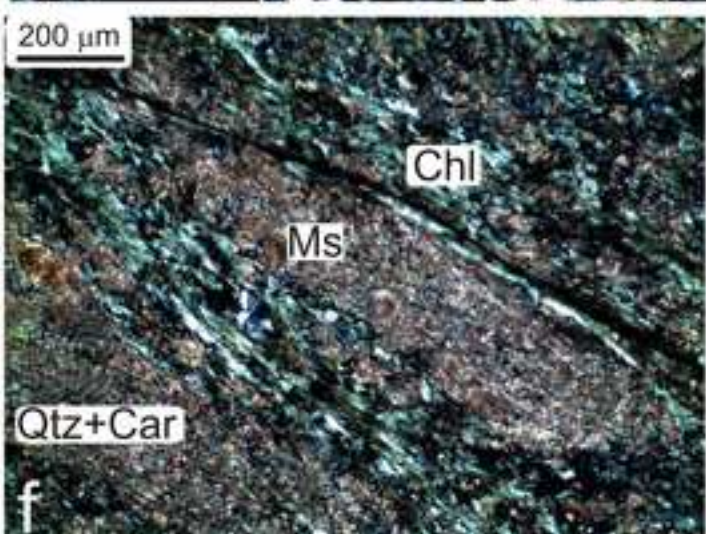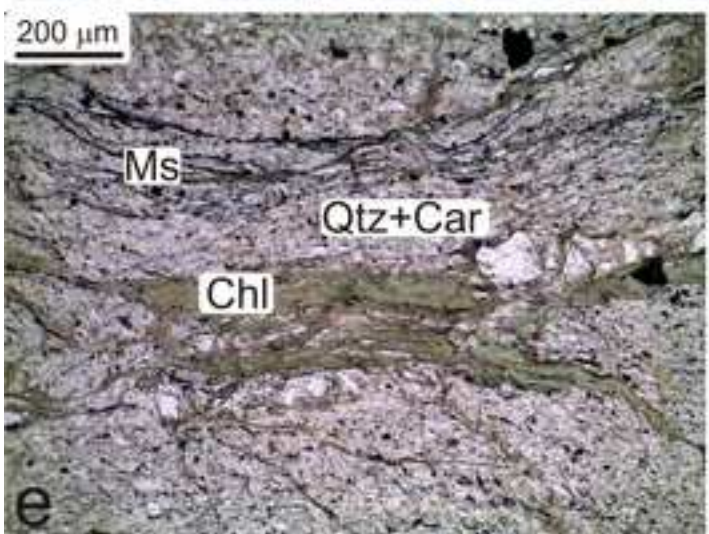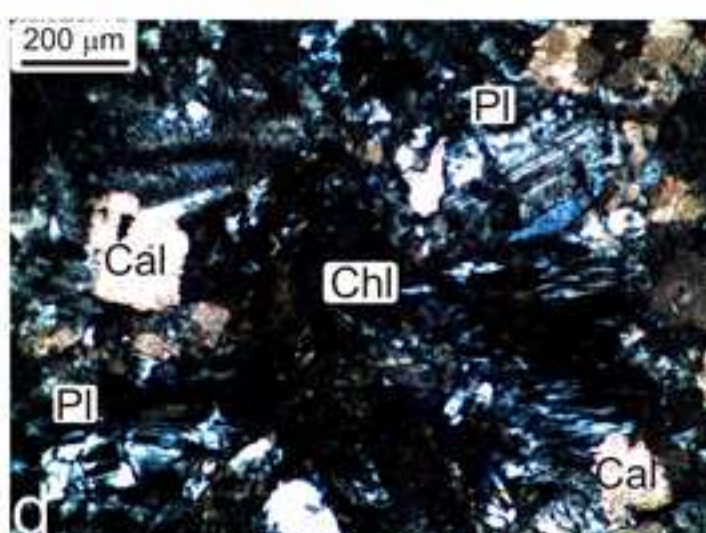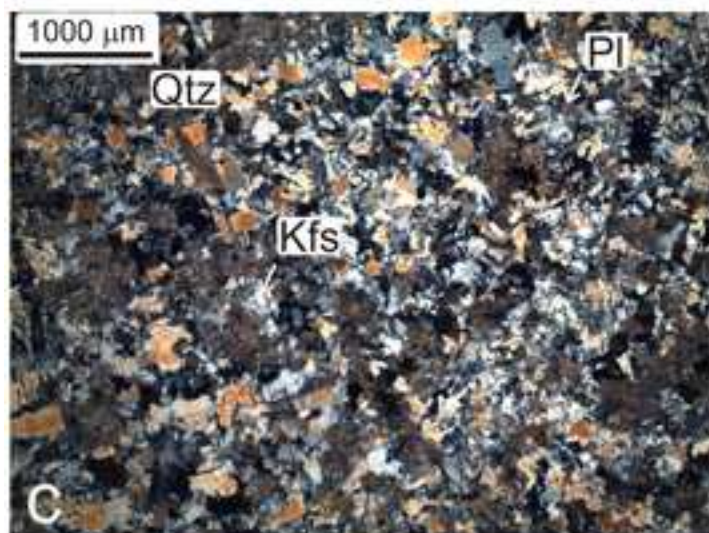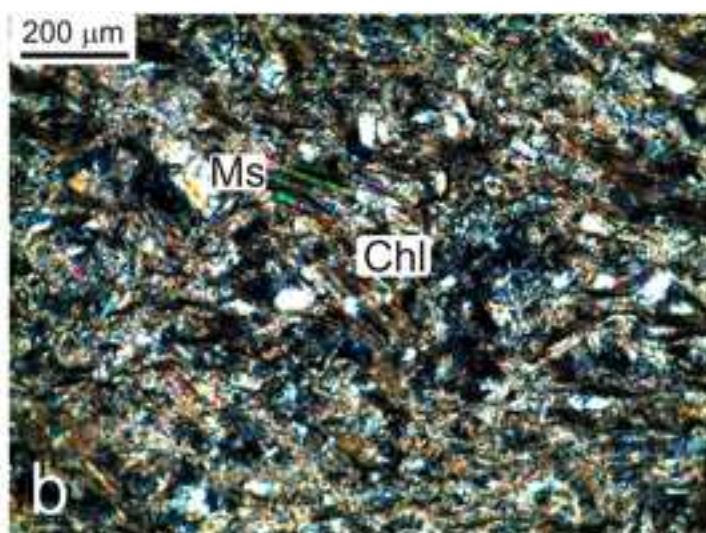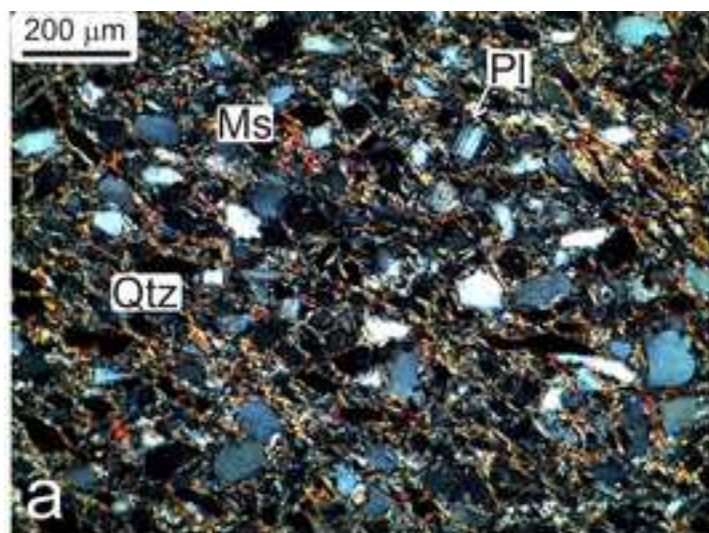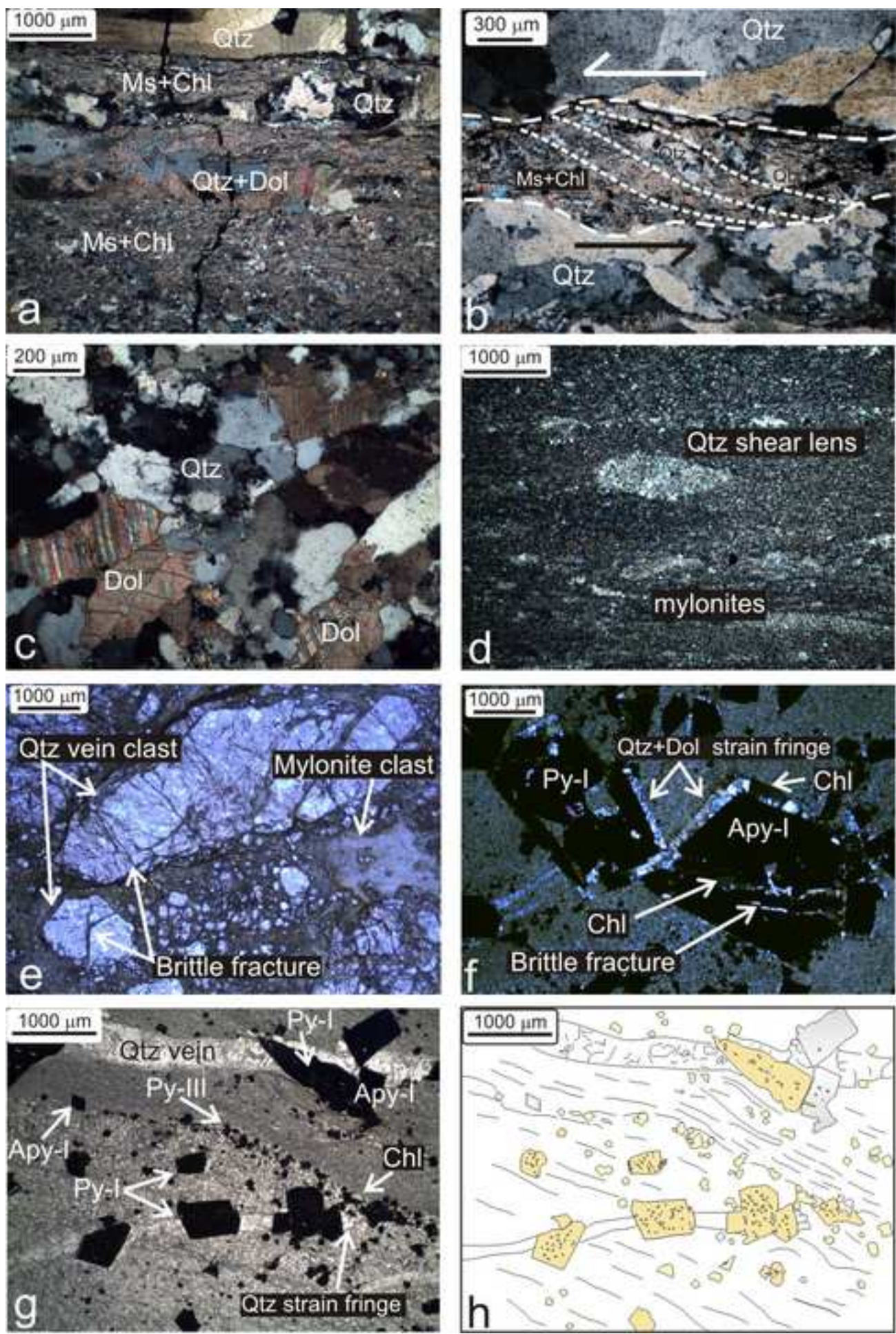
Figure
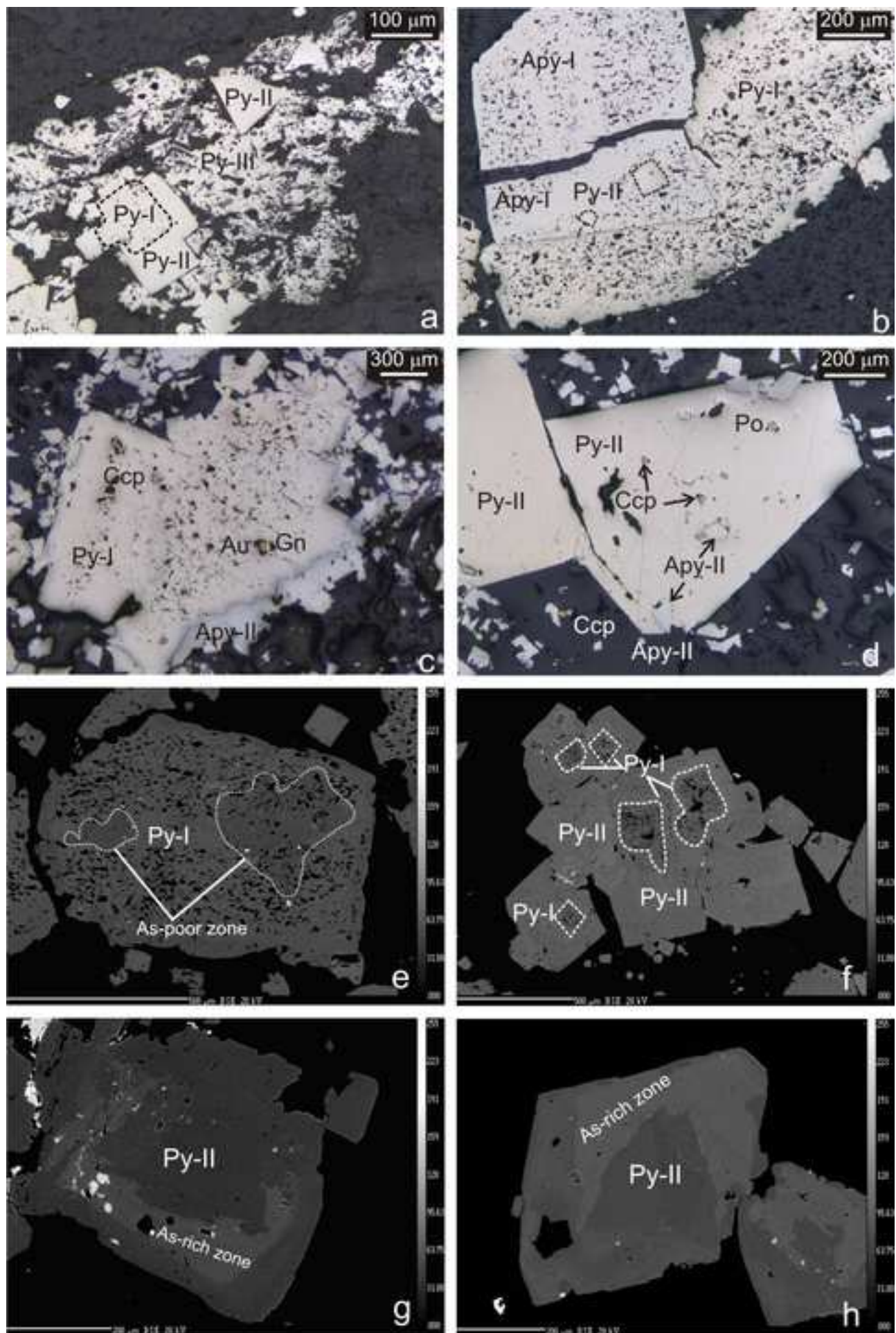
Textural type	Description	Schematic sketch of texture
Arsenopyrite-I	Large euhedral grains with abundant randomly oriented silicate inclusions and may contain inclusions of pyrite-II	
Pyrite-I	Euhedral in shape with numerous randomly to preferentially oriented silicates inclusions and may contain inclusions of sulfides and gold	
Pyrite-II	Euhedral pyrite, almost devoid of silicate inclusions and generally overgrow pyrite-I	
Arsenopyrite-II	Euhedral to subhedral in shape, smaller in size than arsenopyrite-I, free of any silicate inclusions and may overgrow pyrite-I	
Pyrite-III	Irregular grain boundaries and overgrows the shear foliation.	
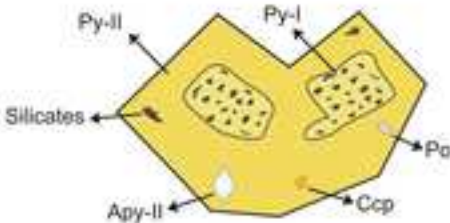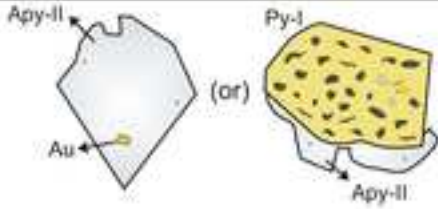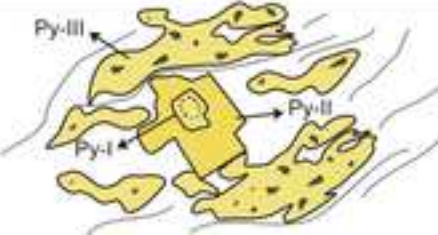
Figure
Click here to download high resolution image
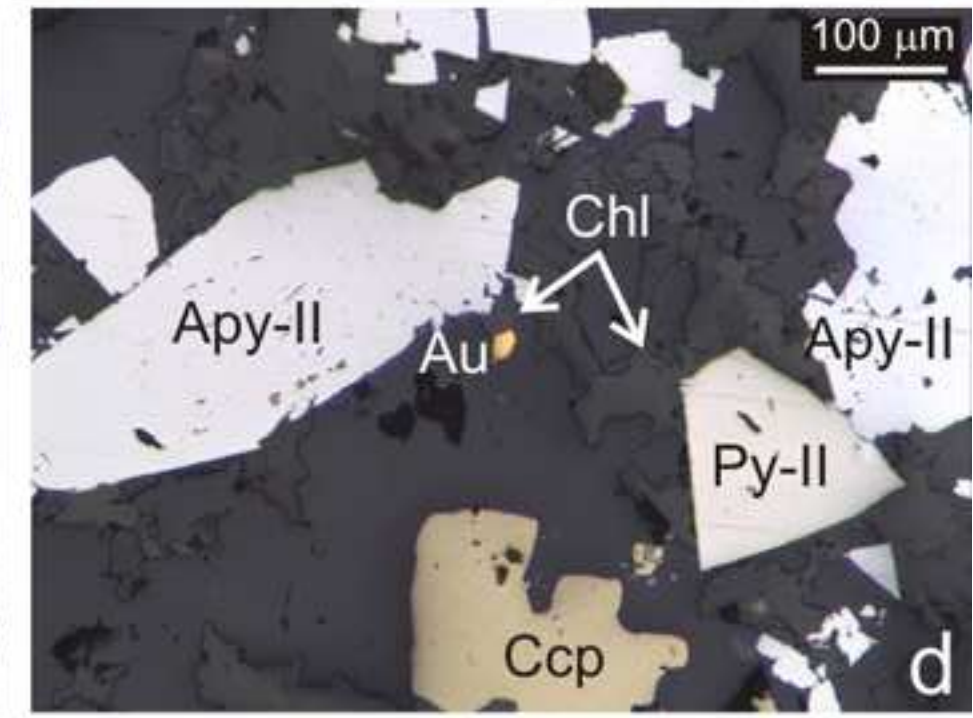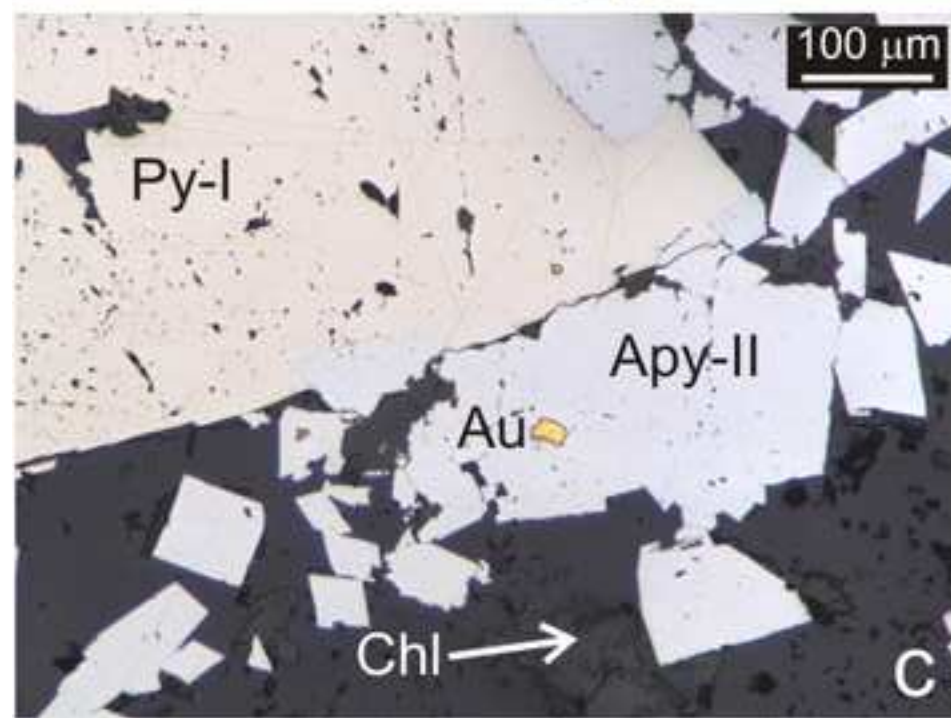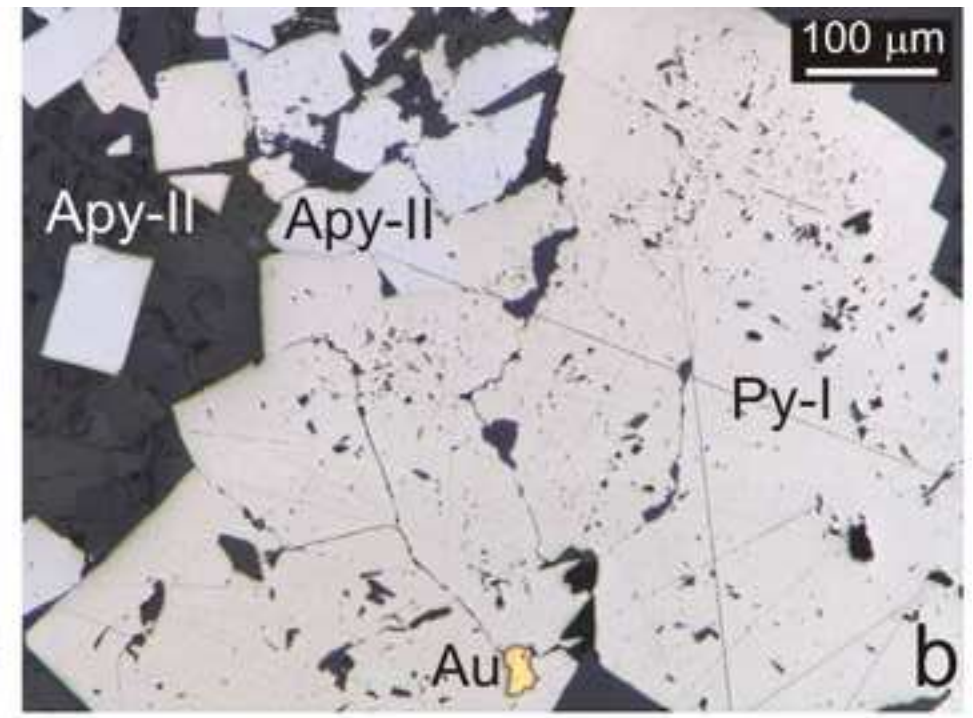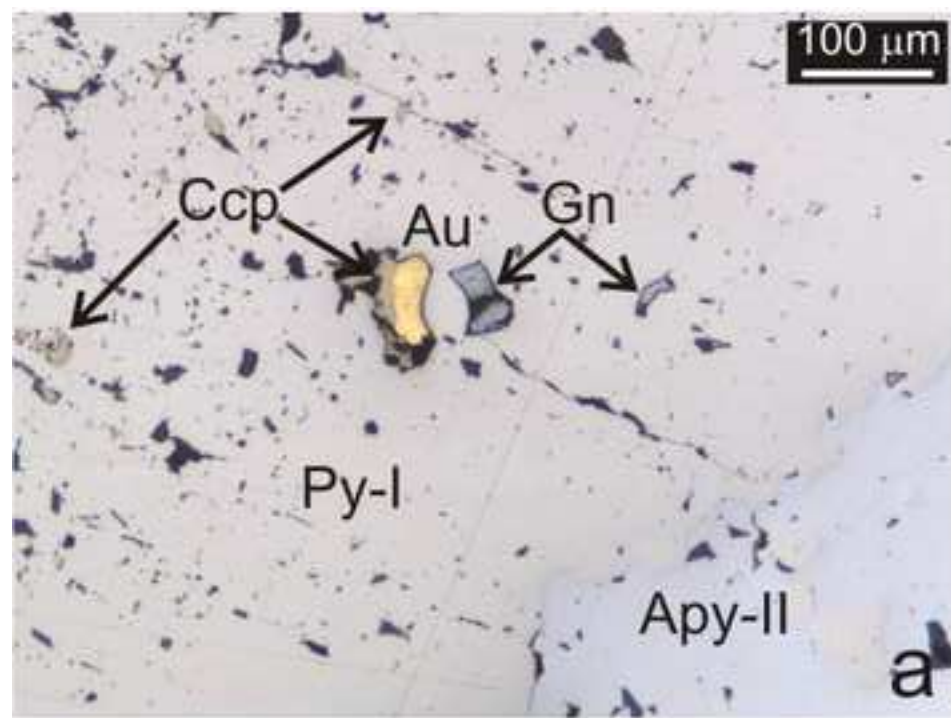
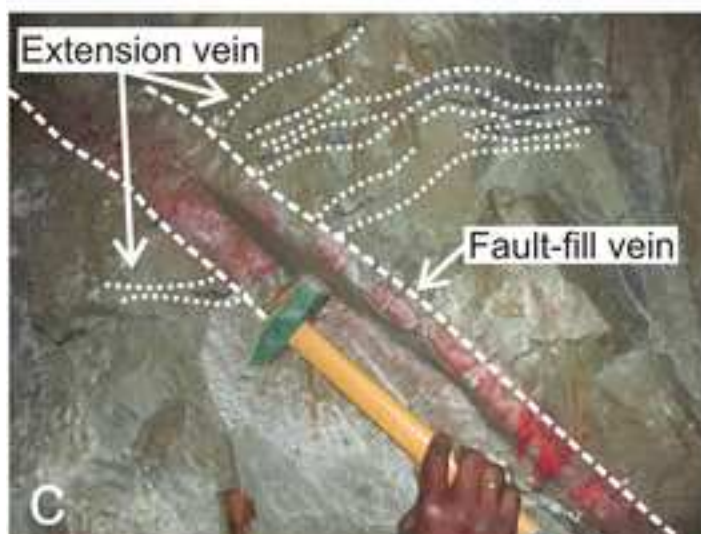data-point error ellipses are 2σ

RO458-4_KU16_Apy

RO458-3_KU16_Py

RO432-2_KUJ1_Apy

RO458-2_KU11_Apy

RO-458-1-KU11_Py
RO432-3KUJ1_Py

Age 2563 ± 84 Ma
Initial $^{187}Os/^{188}Os$ = 0.29 ± 0.08
MSWD = 0.38

$^{187}Os/^{188}Os$

$^{187}Re/^{188}Os$
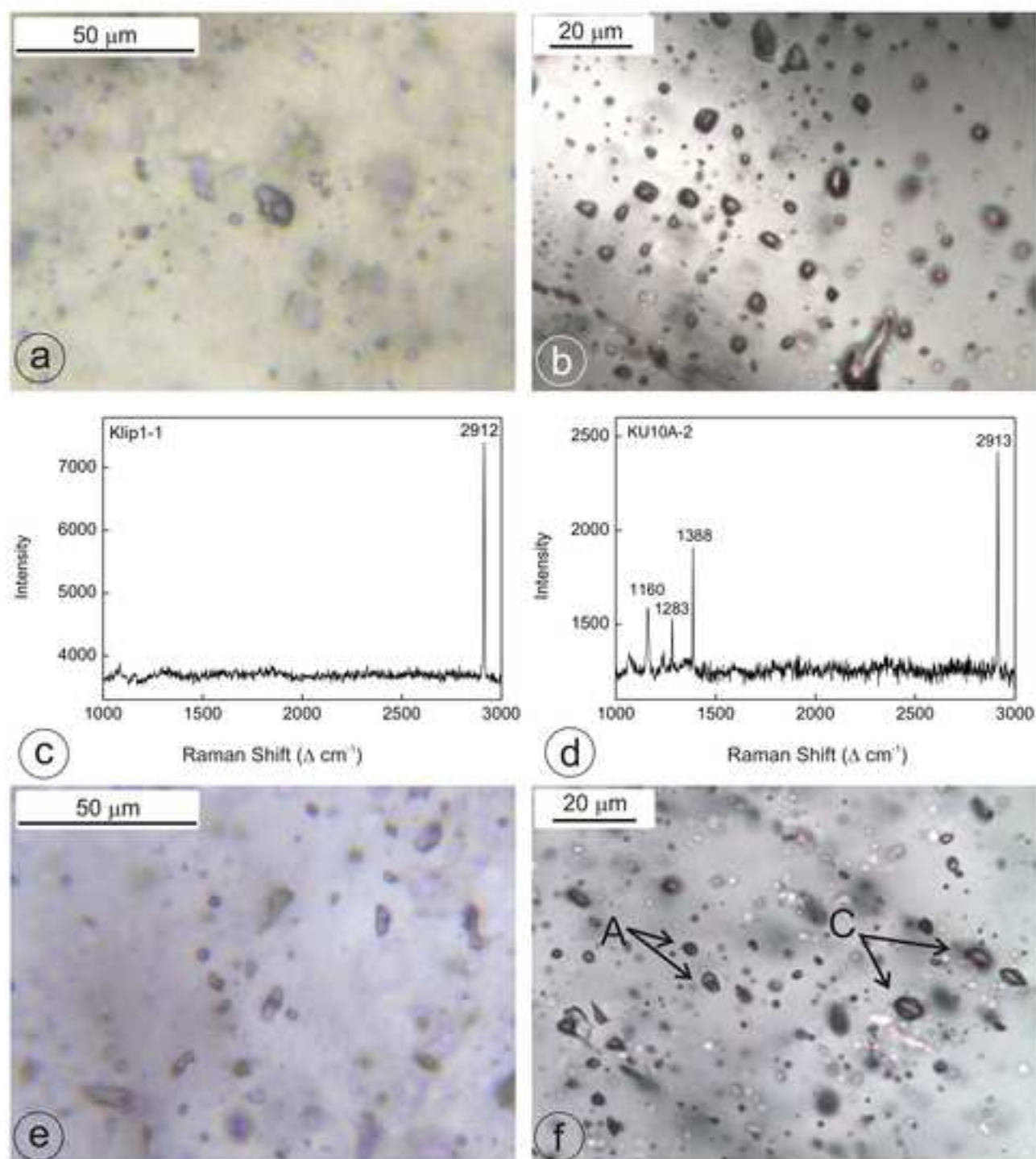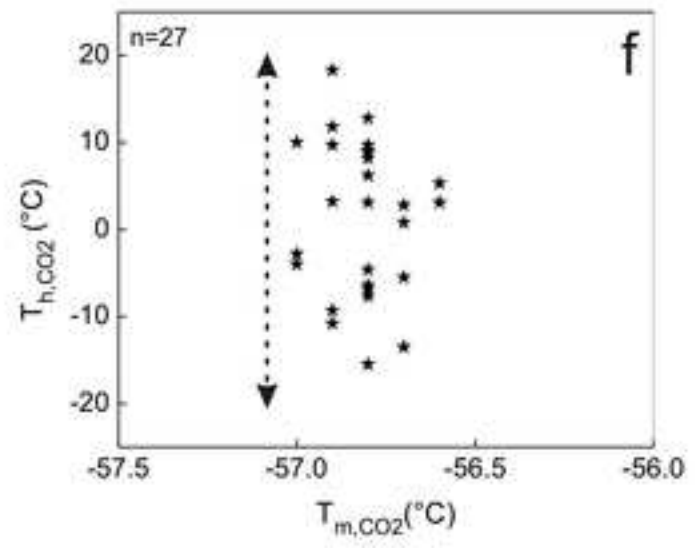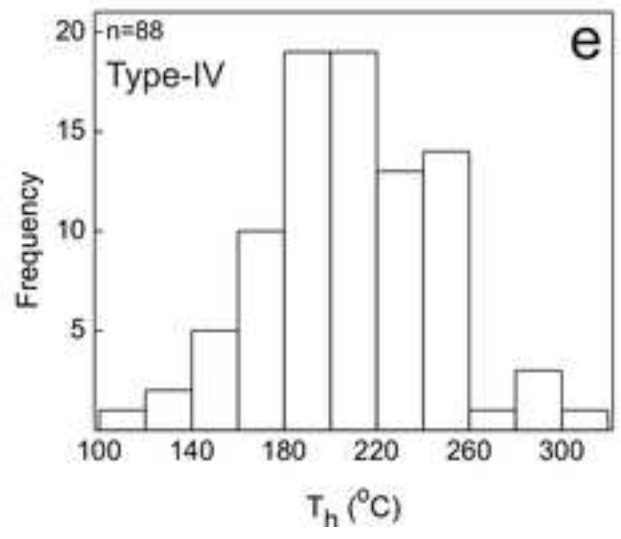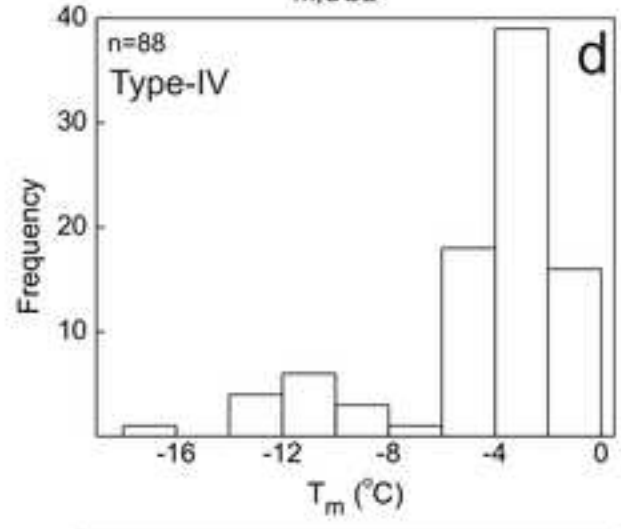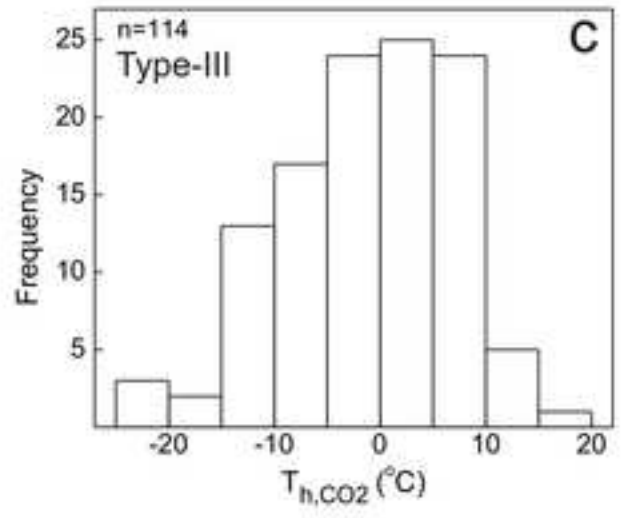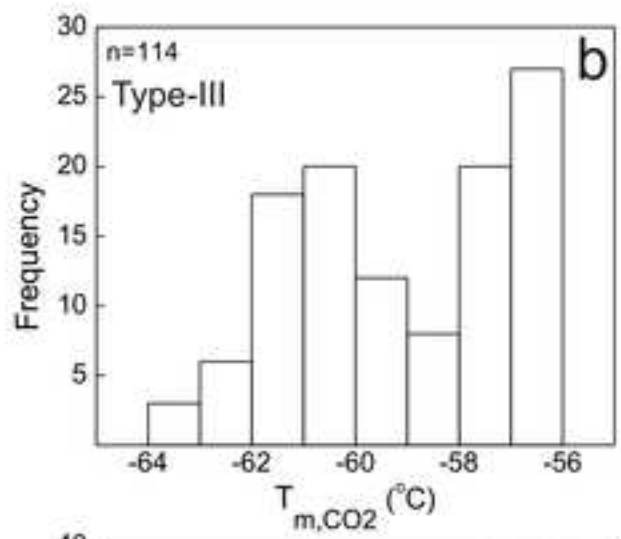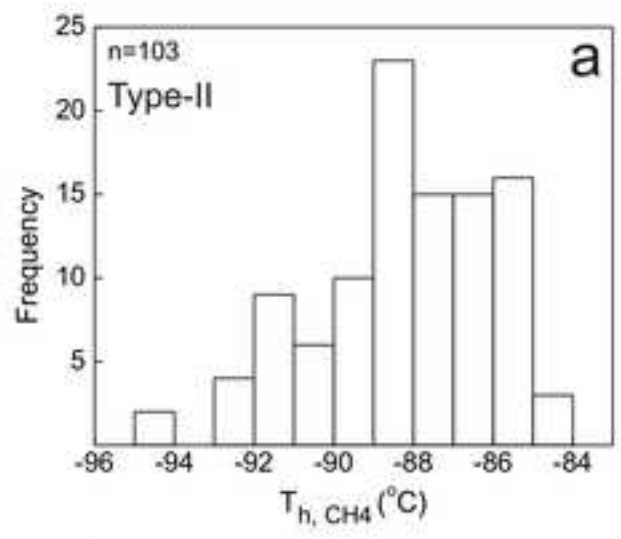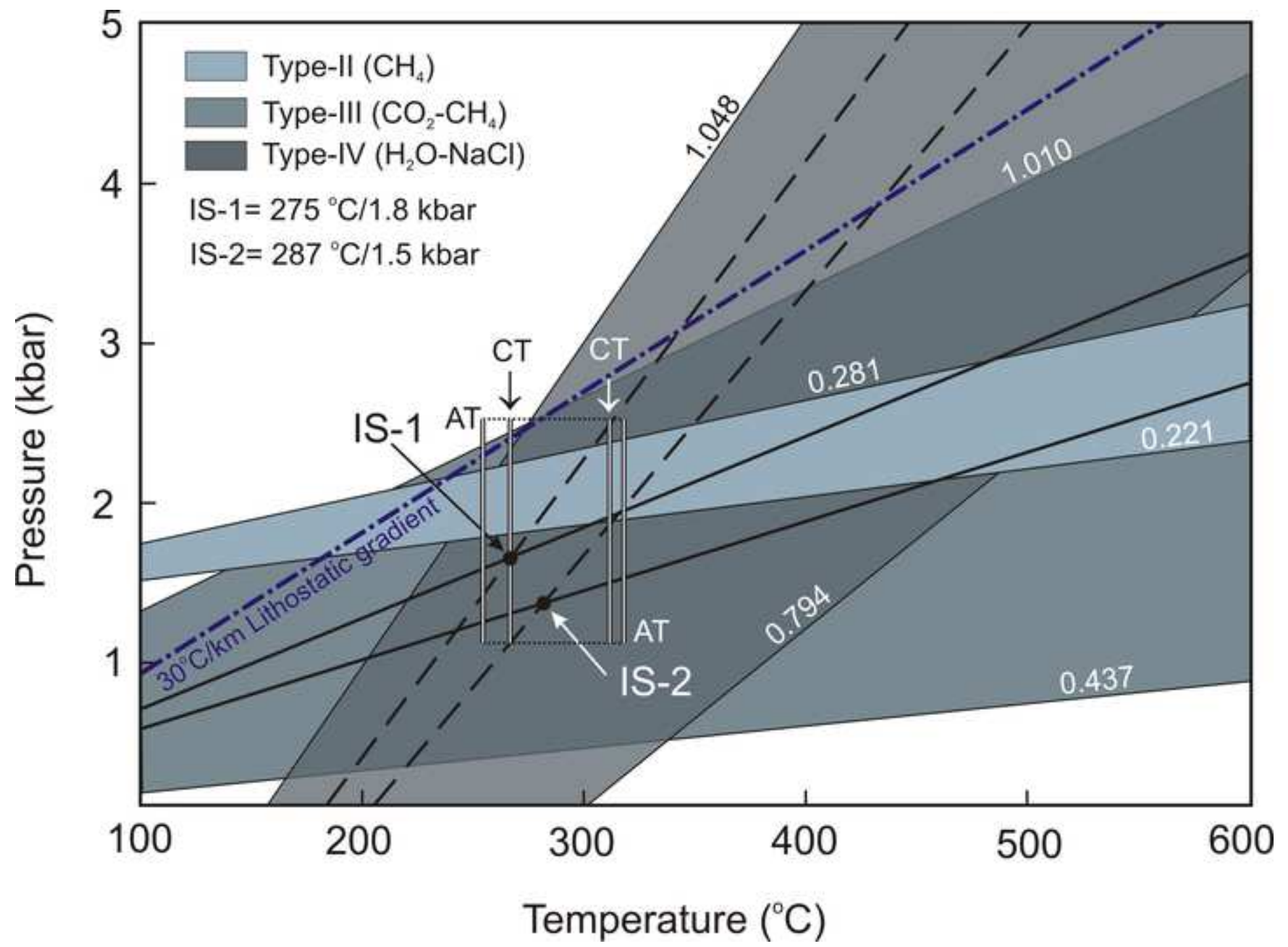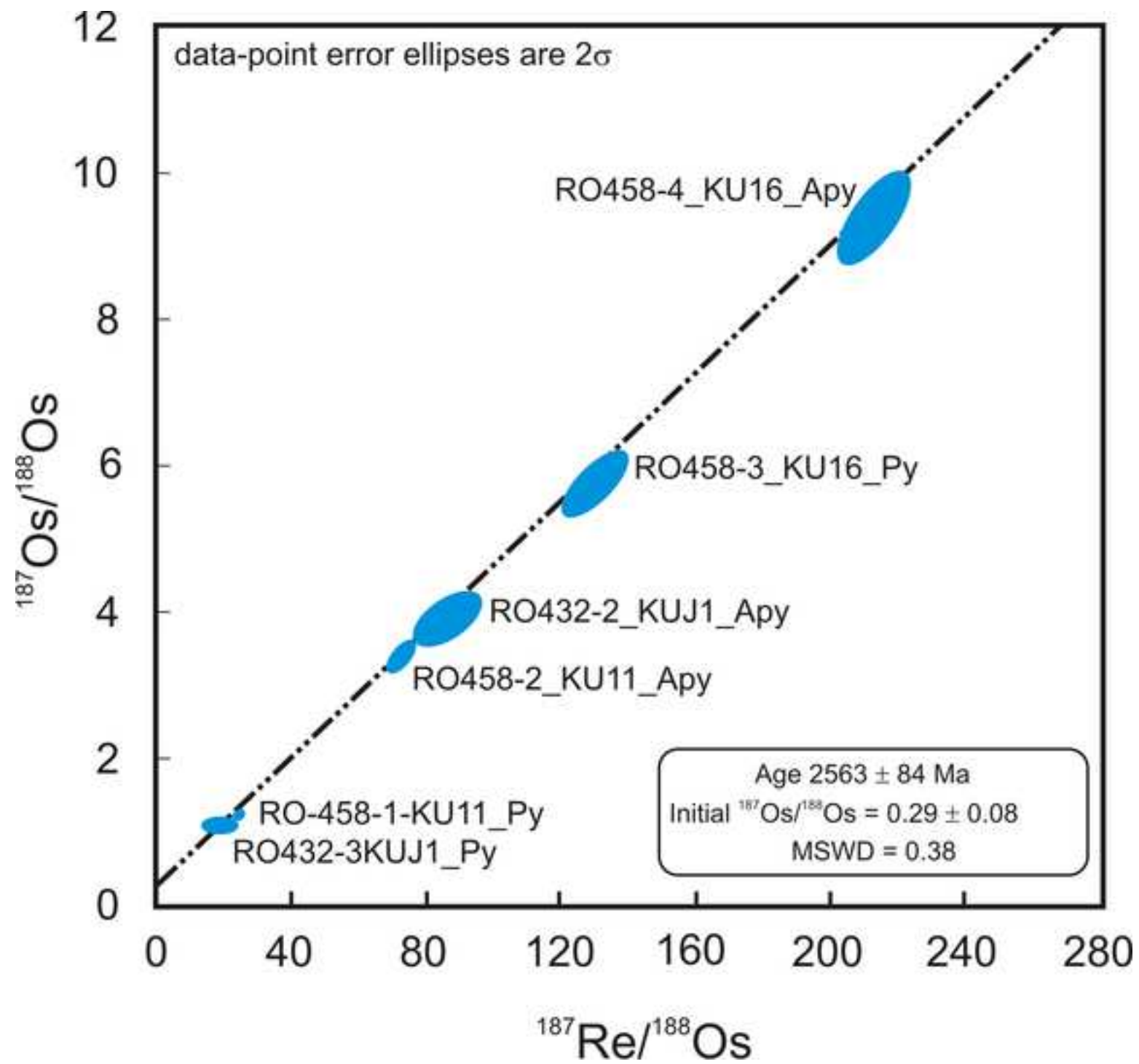
Table. 1. Representative electron probe microanalytical data, structural formulae and estimated temperatures of chlorite from the alteration zones.

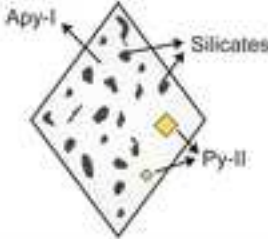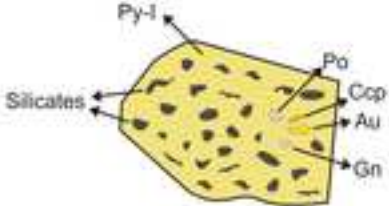|	R-reef												
Sample No	KU4B												
Analysis No	mat-1	mat-2	mat-4	mat-5	py-6	py-7	py-8	py-9	py-10	mat-11	mat-12	mat-13	mat-16
SiO_2	25.62	25.25	25.38	25.51	25.08	26.04	25.21	25.38	25.52	25.78	25.48	26.65	26.82
Al_2O_3	20.88	20.49	20.89	20.17	20.59	20.56	20.48	20.55	20.42	20.75	20.64	18.96	19.42
FeO	27.85	29.21	27.81	27.12	27.74	28.80	28.33	28.97	27.34	28.11	28.10	28.20	28.53
MnO	0.10	0.10	0.11	0.20	0.14	0.00	0.17	0.17	0.13	0.15	0.05	0.11	0.07
MgO	13.63	12.92	13.02	13.47	12.70	13.39	13.17	13.28	13.65	13.65	13.29	14.13	14.04
Total	88.08	87.97	87.21	86.47	86.25	88.79	87.36	88.35	87.06	88.44	87.56	88.05	88.88
Cations													
Si	2.70	2.67	2.72	2.69	2.67	2.69	2.67	2.67	2.69	2.70	2.67	2.73	2.74
Al	2.60	2.55	2.64	2.51	2.59	2.50	2.56	2.54	2.53	2.56	2.55	2.29	2.34
Fe(tot.)	2.46	2.58	2.49	2.39	2.47	2.48	2.51	2.54	2.41	2.46	2.47	2.42	2.43
Mn	0.01	0.01	0.01	0.02	0.01	0.00	0.02	0.02	0.01	0.01	0.00	0.01	0.01
Mg	2.14	2.03	2.08	2.12	2.02	2.06	2.08	2.08	2.14	2.13	2.08	2.16	2.14
Total	9.91	9.84	9.93	9.73	9.76	9.73	9.83	9.85	9.78	9.87	9.78	9.61	9.65
T1 (tetrahedral Al: CN85)	293	300	290	295	300	297	300	301	296	293	299	287	286
T2 (octahedral vacancy: CN85)	270	263	273	250	253	249	262	263	256	266	256	236	240
T3 (tetrahedral Al & Fe/(Fe+Mg): ZF95)	276	269	276	279	276	285	297	272	287	279	282	278	300
Avg. T °C	280	278	280	275	276	277	286	279	280	280	279	267	276
SD	12	20	9	23	23	25	21	20	21	14	22	27	31
Eq. (1)	286	300	287	304	308	312	300	309	300	287	309	300	278
Eq. (2)	317	303	328	292	300	299	306	312	299	308	301	279	269
Eq. (3)	300	300	305	299	306	306	302	310	300	297	306	291	276
Avg.T °C (T4) V01&05	301	301	307	298	305	306	302	310	300	297	305	290	274
SD	16	2	20	6	4	7	3	1	1	11	4	10	5
a(H_2O)	0.3	0.5	0.2	0.9	0.8	1.0	0.5	0.5	0.8	0.5	0.8	0.6	1.0

1

	R-reef														
Sample No	KU4G														
Analysis No	vein-1	vein-2	vein-3	vein-4	vein-5	vein-6	vein-7	vein-8	vein-9	vein-10	mat-11	mat-12	mat-13	mat-14	mat-15
SiO_2	24.25	24.23	24.33	24.16	24.23	24.18	24.27	24.49	24.70	24.50	24.37	24.85	24.60	24.38	22.93
Al_2O_3	18.46	18.81	18.82	18.35	18.87	18.72	18.82	18.61	18.51	18.37	18.96	19.33	18.38	18.93	18.03
FeO	36.32	36.69	36.91	36.25	36.49	36.50	36.50	36.32	36.45	36.62	36.68	36.78	37.15	36.44	35.33
MnO	0.13	0.04	0.01	0.08	0.09	0.08	0.11	0.12	0.09	0.19	0.06	0.16	0.05	0.00	0.33
MgO	7.78	7.62	7.56	7.79	7.74	7.67	7.68	7.97	8.06	7.90	7.75	8.26	7.59	7.90	7.36
Total	86.94	87.39	87.63	86.63	87.42	87.15	87.38	87.51	87.81	87.58	87.82	89.38	87.77	87.65	83.98
Cations															
Si	2.67	2.67	2.67	2.68	2.66	2.67	2.67	2.67	2.68	2.68	2.67	2.66	2.68	2.67	2.67
Al	2.39	2.44	2.44	2.40	2.45	2.44	2.44	2.39	2.37	2.37	2.45	2.44	2.36	2.45	2.47
Fe(tot.)	3.34	3.38	3.39	3.37	3.36	3.37	3.36	3.32	3.31	3.35	3.36	3.30	3.39	3.34	3.44
Mn	0.01	0.00	0.00	0.01	0.01	0.01	0.01	0.01	0.01	0.02	0.01	0.01	0.00	0.00	0.03
Mg	1.28	1.25	1.24	1.29	1.27	1.26	1.26	1.30	1.31	1.29	1.27	1.32	1.23	1.29	1.28
Total	9.69	9.74	9.74	9.75	9.74	9.75	9.74	9.69	9.68	9.69	9.75	9.74	9.68	9.75	9.89
T1 (tetrahedral Al: CN85)	301	300	299	297	301	300	300	299	297	299	300	301	297	300	300
T2 (octahedral vacancy: CN85)	245	251	251	252	251	252	251	246	244	245	252	251	244	252	269
T3 (tetrahedral Al& Fe/(Fe+Mg): ZF95)	302	303	304	305	306	307	308	309	310	311	312	313	314	315	316
Avg. T °C	*283*	*285*	*285*	*285*	*286*	*286*	*286*	*285*	*284*	*285*	*288*	*288*	*285*	*289*	*295*
SD	33	29	30	29	30	30	31	34	35	35	32	33	37	33	24
Eq. (1)	314	314	306	301	320	317	314	321	311	316	308	312	310	311	286
Eq. (2)	286	298	292	292	302	300	299	292	290	292	292	298	288	296	301
Eq. (3)	301	306	300	298	313	311	307	308	301	306	301	306	300	305	292
Avg.T °C (T4) V01&05	*301*	*306*	*299*	*297*	*312*	*309*	*307*	*307*	*300*	*305*	*300*	*305*	*299*	*304*	*293*
SD	14	8	7	5	9	9	8	14	10	12	8	7	11	8	8
a(H_2O)	0.8	1.0	1.0	1.0	1.0	1.0	1.0	0.9	1.0	0.9	0.9	0.9	1.0	1.0	0.3

2

	J reef				
Sample No	KU12B				
Analysis No	1	2	3	5	7
SiO$_2$	25.49	23.94	25.64	24.69	24.89
Al$_2$O$_3$	18.44	21.41	18.52	20.78	19.80
FeO	33.87	33.70	33.09	34.06	34.24
MnO	0.00	0.02	0.13	0.00	0.00
MgO	9.40	7.97	9.65	7.75	8.90
Total	87.20	87.04	87.03	87.28	87.83
Cations					
Si	2.74	2.66	2.84	2.68	2.68
Al	2.33	2.80	2.41	2.65	2.52
Fe(tot.)	3.04	3.13	3.06	3.09	3.09
Mn	0.00	0.00	0.01	0.00	0.00
Mg	1.50	1.32	1.59	1.25	1.43
Total	9.62	9.92	9.92	9.67	9.72
T1 (tetrahedral Al: CN85)	286	302	265	299	297
T2 (octahedral vacancy: CN85)	236	272	271	242	248
T3 (tetrahedral Al& Fe/(Fe+Mg): ZF95)	318	319	320	321	322
Avg. T °C	*280*	*298*	*286*	*288*	*289*
SD	41	24	30	41	38
Eq. (1)	279	277	247	299	291
Eq. (2)	264	296	323	274	279
Eq. (3)	273	284	277	288	285
Avg.T °C (T4) V01&05	*272*	*286*	*282*	*287*	*285*
SD	7	9	38	13	6
a(H$_2$O)	1.0	0.2	1.0	1.0	1.0

		J reef										
Sample No		KUJ1										
Analysis No		1	2	3	4	5	6	7	8	9	10	11	12
SiO_2		26.03	25.86	25.94	25.55	26.59	26.39	26.30	25.81	26.01	25.94	25.77	25.99
Al_2O_3		20.51	20.71	20.65	20.60	20.35	20.01	20.03	20.77	21.40	20.15	21.18	21.03
FeO		24.81	25.42	26.21	26.40	26.07	25.89	26.43	25.18	25.88	25.99	26.07	25.26
MnO		0.00	0.05	0.05	0.05	0.00	0.06	0.11	0.00	0.00	0.16	0.04	0.00
MgO		15.11	15.06	15.10	14.61	15.31	15.38	15.17	15.22	15.11	15.26	15.06	15.20
Total		86.46	87.10	87.95	87.21	88.32	87.73	88.04	86.98	88.40	87.50	88.12	87.48
Cations													
Si		2.70	2.68	2.72	2.68	2.71	2.70	2.70	2.71	2.70	2.72	2.69	2.69
Al		2.51	2.53	2.55	2.55	2.45	2.41	2.42	2.57	2.62	2.49	2.61	2.57
Fe(tot.)		2.15	2.21	2.30	2.32	2.22	2.22	2.27	2.21	2.25	2.28	2.28	2.19
Mn		0.00	0.00	0.00	0.00	0.00	0.01	0.01	0.00	0.00	0.01	0.00	0.00
Mg		2.34	2.33	2.36	2.28	2.33	2.35	2.32	2.38	2.34	2.39	2.35	2.35
Total		9.70	9.76	9.93	9.83	9.71	9.69	9.72	9.88	9.92	9.90	9.93	9.79
T1 (tetrahedral Al: CN85)		293	297	290	298	291	293	294	291	293	289	295	295
T2 (octahedral vacancy: CN85)		247	253	273	262	247	245	249	267	271	270	273	257
T3 (tetrahedral Al& Fe/(Fe+Mg): ZF95)		324	325	326	327	328	329	330	331	332	333	334	335
Avg. T °C		*288*	*292*	*296*	*296*	*289*	*289*	*291*	*297*	*299*	*297*	*301*	*296*
SD		39	36	27	33	41	43	41	33	31	33	31	39
Eq. (1)		300	278	287	283	269	281	277	282	297	262	299	274
Eq. (2)		287	276	325	296	268	268	275	307	323	299	327	279
Eq. (3)		295	277	304	289	268	276	276	292	307	277	311	276
Avg.T °C (T4) V01&05		*294*	*277*	*305*	*289*	*268*	*275*	*276*	*294*	*309*	*279*	*312*	*276*
SD		6	1	19	6	1	6	1	13	13	19	14	3
$a(H_2O)$		1.0	0.6	0.2	0.4	0.8	0.7	0.7	0.5	0.3	0.3	0.3	0.2

Note: CN85: Cathelineau and Nieva (1985); ZF95: Zang and Fyfe (1995); V01&05: Vidal et al. (2001) and (2005)

4

Table. 2. Selected electron probe microanalytical data of arsenopyrite from alteration zones along with results of arsenopyrite thermometry after Kretschmar and Scot (1976) and Sharp et al. (1985).

Sample No	KU10A																		
Analysis No	2	3	4	8	11	12	13	14	16	17	18	22	23	25	26	27	28	30	31
Fe	36.12	36.26	36.47	36.63	36.65	36.77	36.37	36.26	36.35	36.47	36.82	36.55	36.55	36.72	36.14	36.67	36.82	36.33	36.57
As	41.46	40.85	41.06	41.08	41.55	41.20	41.77	40.85	42.10	42.09	41.05	41.28	41.75	41.61	42.45	41.29	41.10	41.16	40.99
S	22.72	22.68	22.90	22.80	22.52	22.59	22.40	22.90	22.34	22.22	22.74	22.55	22.39	22.45	21.97	22.86	22.95	22.75	22.84
Co	0.04	0.00	0.00	0.04	0.02	0.02	0.00	0.00	0.00	0.00	0.00	0.00	0.01	0.00	0.01	0.00	0.00	0.00	0.01
Ni	0.11	0.00	0.00	0.00	0.11	0.00	0.01	0.00	0.01	0.00	0.00	0.00	0.00	0.00	0.00	0.00	0.00	0.00	0.00
Cu	0.00	0.00	0.00	0.00	0.00	0.00	0.02	0.00	0.00	0.00	0.00	0.01	0.00	0.00	0.00	0.00	0.00	0.00	0.00
Zn	0.00	0.00	0.00	0.00	0.00	0.00	0.03	0.00	0.00	0.00	0.00	0.00	0.00	0.00	0.00	0.00	0.01	0.00	0.00
Ga	0.00	0.00	0.01	0.00	0.03	0.01	0.00	0.01	0.03	0.01	0.01	0.00	0.00	0.00	0.00	0.00	0.00	0.00	0.00
Se	0.16	0.18	0.10	0.18	0.18	0.15	0.12	0.17	0.18	0.13	0.13	0.14	0.14	0.15	0.13	0.22	0.15	0.17	0.15
Ag	0.00	0.00	0.00	0.00	0.00	0.00	0.00	0.00	0.01	0.00	0.01	0.00	0.00	0.00	0.00	0.01	0.00	0.00	0.00
Au	0.00	0.00	0.00	0.07	0.00	0.00	0.00	0.00	0.01	0.00	0.01	0.05	0.00	0.00	0.00	0.00	0.00	0.00	0.04
Total	100.61	99.98	100.54	100.78	101.05	100.73	100.73	100.19	101.03	100.92	100.76	100.58	100.83	100.92	100.69	101.05	101.03	100.42	100.61
As %	28.9	28.6	28.6	28.6	28.9	28.7	29.2	28.5	29.4	29.4	28.6	28.8	29.1	29.0	29.8	28.6	28.5	28.7	28.5
T (°C)	277	265	265	265	277	267	291	260	300	300	265	272	286	282	318	265	260	267	260

Sample No	KU16										
Analysis No	3	4	5	6	8	10	11	13	16	17	19
Fe	36.02	35.91	36.23	35.86	36.35	36.31	36.34	35.54	36.24	36.14	36.43
As	41.40	41.11	41.10	41.20	41.19	40.85	40.89	40.74	41.54	40.91	40.85
S	22.29	22.57	22.59	22.51	22.54	22.75	22.54	22.71	22.13	22.69	22.64
Co	0.00	0.02	0.00	0.01	0.00	0.01	0.01	0.01	0.00	0.00	0.00
Ni	0.00	0.01	0.00	0.00	0.00	0.00	0.00	0.00	0.00	0.00	0.00
Cu	0.00	0.00	0.00	0.00	0.00	0.00	0.00	0.00	0.00	0.00	0.00
Zn	0.00	0.00	0.00	0.00	0.00	0.00	0.00	0.00	0.00	0.00	0.00
Ga	0.00	0.00	0.00	0.00	0.00	0.00	0.02	0.00	0.00	0.02	0.04
Se	0.13	0.15	0.13	0.17	0.15	0.17	0.13	0.09	0.17	0.16	0.16
Ag	0.00	0.00	0.00	0.00	0.00	0.00	0.00	0.00	0.00	0.00	0.00
Au	0.00	0.00	0.04	0.00	0.00	0.03	0.00	0.00	0.00	0.04	0.03
Total	99.84	99.77	100.09	99.75	100.23	100.12	99.93	99.08	100.08	99.97	100.14
As %	29.0	28.8	28.7	28.8	28.7	28.4	28.5	28.6	29.1	28.5	28.4
T (°C)	282	272	262	272	262	255	260	265	286	260	255

Table. 3. Summary of fluid inclusion microthermometric data.

Sample No (Reef)	Type	n	T_{m,CO_2} (°C)	T_{h,CO_2} (°C)	T_{h,CH_4} (°C)	$T_{m,Cl}$ (°C)	$T_{m,ice}$ (°C)	T_h (°C)	$T_{h,tot}$ (°C)	$X_{(CO_2)}$	$X_{(CH_4)}$	V_g(%)	Density (g/cm^3)
Klip-1 (R-reef)	I	12	-62.5 to -57.8	-12.6 to 7.8		9.2 to 13.5			299 to 367	0.25 to 0.75	0.03 to0.25	40 to 90	0.356 to 0.805
	II	31			-92.8 to -84.3					0.00	1.00		0.221 to 0.275
	III	33	-62.8 to -56.6	-13.1 to 9.1						0.73 to 1.0	0.27 to 0.0		0.663 to 0.971
	IV	22					-16.1 to -0.2	115 to 292					0.799 to 1.048
KU16 (R-reef)	II	20			-94.3 to -85.2								0.230 to 0.281
	III	25	-63.5 to-56.8	-15.5 to 18.3						0.69 to 1	0 to 0.31		0.690 to 1.010
	IV	19					-4.6 to -1.9	172 to 299					0.794 to 0.947
KU10A (J-reef)	I	9	-63.2 to -58.2	-15.2 to 0.5		7.8 to 14.8			272 to 345	0.71 to 0.95	0.05 to 0.29	70 to 90	0.352 to 0.713
	II	12			-91.9 to -84.8								0.226 to 0.271
	III	17	-63.9 to -60.0	-20.1 to 0.2									0.642 to 0.831
	IV	15					-10.3 to -0.3	205 to 302					0.803 to 0.935
KU12D (J-reef)	II	25			-94.2 to -85.4								0.232 to 0.280
	III	19	-60.2 to -56.7	-13.5 to 13.4						0.86 to 1.0	0.0 to 0.14		0.437 to 1.001
	IV	15					-12.2 to -2.0	157 to 222					0.901 to 0.982
KU9C (H-reef)	II	15			-92.5 to -84.9								0.227 to 0.273
	III	20	-63.0 to -57.2	-14.8 to 13.0						0.72 to 0.99	0.01 to 0.29		0.645 to 0.972
	IV	17					-12.5 to -0.5	130 to 250					0.831 to 1.022

Table 4. Re-Os pyrite and arsenopyrite data.

Sample No	Location	Mineral	Re (ppb)	±	Os (ppt)	±	^{192}Os (ppt)	±	^{187}Re/^{188}Os	±	^{187}Os/^{188}Os	±	rho
RO432-2_KUJI_Apy	J-Reef	Arsenopyrite	0.9	0.1	73.4	2.4	20.3	1.4	84.1	8.1	3.9337	0.3161	0.626
RO432-3_KUJI_Py	J-Reef	Pyrite	0.2	0.1	56.6	1.7	20.7	1.5	18.7	5.7	1.1147	0.0905	0.193
RO458-1_KU11_Py	H-Reef	Pyrite	0.4	0.0	106.6	2.2	38.3	1.6	22.4	1.2	1.2645	0.0725	0.552
RO458-2_KU11_Apy	H-Reef	Arsenopyrite	1.6	0.0	154.1	3.9	44.4	1.8	70.6	3.0	3.4446	0.1967	0.692
RO458-3_KU16_Py	R-Reef	Pyrite	0.5	0.0	32.5	1.0	7.7	0.4	128.1	8.1	5.7947	0.3978	0.715
RO458-4_KU16_Apy	R-Reef	Arsenopyrite	4.7	0.0	240.4	8.0	44.8	1.8	210.4	8.6	9.4437	0.5389	0.708

Note: Uncertainties are reported at the 2σ level. ^{187}Os/^{188}Os uncertainties are at 2SE. All data are blank corrected, blanks for Os and Re were 0.1 ± 0.1 and 6.2 ± 5.4 ppt respectively, with an average ^{187}Os/^{188}Os value of 0.25 ± 0.02 (1 SD, n = 2).

Table. 5. Summery of ore fluid compositions and P-T conditions of gold mineralization in major orogenic gold deposits around the world.

Age	Gold fields/ deposits	Cratons/regions	Fluid composition	Salinity (wt.% NaCl equiv.)	Mineralizing P-T conditions	References
Early Paleocene – Early Eocene	Alaska–Juneau, Treadwell Kensington	Juneau gold belt, SE Alaska	$H_2O-CO_2-CH_4-NaCl$	NA	250 to 350°C and 0.75 to 3 kbar	Goldfarb et al. (1993)
Siluro-Devonian	Hodgkinson gold field	NE Austraila,		3 to 11	270 to 355°C and ~1 kbar	Peters et al. (1990); Bierlein and Crowe (2000)
Cambro-Orodovician	Lachlan gold field	SE Australia		NA	250 to 350°C	Gao and Kwak (1995a, b); Ramsay et al. (1998)
Late – Middle Archaean	Willuna gold camp	Yilgarn Craton, western Australia	$H_2O-CO_2-CH_4-NaCl$ with varying CO_2-CH_4 ratio	2.9±2.1	300±30°C and 0.55 to 1.4 kbar	Hagemann et al. (1994, 1996)
	Kalgoorlie camp, Golden Mile			NA	264 to 360°C and 1.5 to 2.3 kbar.	Ho (1987); Ho et al. (1990); Hagemann and Cassidy (2000)
	Mount Charlotte deposit			≤5		Hagemann and Cassidy (2000); Mernagh (1996)
	Hollinger-McIntyre deposit	Abitibi sub-province at Timmins district, Canada	$H_2O-CO_2-CH_4-NaCl$	NA	277±48°C	Smith et al. (1984); Spooner et al. (1987)
	Sigma-Lamaque, Val d'Or		$H_2O-CO_2-CH_4-NaCl$ with 15−30 mole % CO_2	<10	1.8 to 2.6 kbar	Hagemann and Brown (1996); Robert and Kelly (1987)
	Barberton greenstone belt	Kappval Craton, South Africa	$H_2O-CO_2-CH_4-NaCl$	NA	~300°C and 1 kbar.	de Ronde et al. (1992)
	Kolar gold field	Eastern Dharwar Craton, India	H_2O-CO_2-NaCl	~7	205 to 280°C and 0.7 to 1.8 kbar	Mishra and Panigraghi (1999)
	Hutti gold mine, Hutti-Muski greenstone belt		$H_2O-CO_2-CH_4-NaCl$	3.9–13.5	280–320°C and 1.0 to 1.7 kbar	Pal and Mishra (2002); Mishra and Pal (2008)
	Hira-Buddini mine, Hutti-Muski greenstone belt			0.5 to 22.7	550°C[1] 320°C[2]	[1]Krienitz et al. (2008) [2]Mishra and Pal (2008)
	Ramagiri gold field		Dominantly carbonic fluids	low-salinity	1.45 kbar/240°C to 1.7 kbar/267°C;	Sinha (1997)
	Jonnagiri Deposit, Jonnagiri greenstone belt		$H_2O-CO_2-CH_4-NaCl$	~5	263 – 323°C and 1.4 to 2.5 kbar	Saravanan et al. (2009); Chinnasamy and Mishra (2013)

Note: NA= Not available